POES MEPED differential flux retrievals and electron channel contamination correction

E. D. Peck [1, 2], C. E. Randall [1, 2], J. C. Green [3], J. V. Rodriguez [4, 5], C. J. Rodger [6]

1. Laboratory for Atmospheric and Space Physics, University of Colorado Boulder, Boulder, Colorado, USA.

2. Department of Atmospheric and Oceanic Sciences, University of Colorado Boulder, Boulder, Colorado, USA.

3. Space Hazards Applications, LLC, Golden, Colorado, USA.

4. Cooperative Institute for Research in Environmental Sciences, University of Colorado Boulder, Boulder, Colorado, USA.

5. National Centers for Environmental Information, National Oceanic and Atmospheric Administration, Boulder, Colorado, USA.

6. Department of Physics, University of Otago, Dunedin, New Zealand.

Abstract

A correction method to remove proton contamination from the electron channels of the Polar-orbiting Operational Environmental Satellites (POES) Medium Energy Proton/Electron Detector (MEPED) is described. Proton contamination estimates are based on measurements in five of the MEPED proton spectral channels. A constrained inversion of the MEPED proton channel response function matrix is used to calculate proton differential flux spectra. In this inversion, the proton energy distribution is described by a weighted combination of exponential, power law and Maxwellian distributions. Proton contamination in the MEPED electron spectral channels is derived by applying the electron channel proton sensitivities to the proton fluxes from the best fit

proton spectra. Once the electron channel measurements are corrected for proton contamination, an inversion of the electron channel response function matrix is used to calculate electron differential flux spectra. A side benefit of the method is that it yields an estimate for the integrated electron flux in the energy range from 300 keV to 2.5 MeV with a center energy at ~800 keV. The final product is a differential spectrum of electron flux covering the energy range from about 10 keV to 2.5 MeV that is devoid of proton contamination except during large solar proton events. Comparisons of corrected MEPED differential fluxes to the Detection of Electromagnetic Emissions Transmitted from Earthquake Regions (DEMETER) Instrument for Detecting Particles (IDP) shows that MEPED fluxes are greater than what is expected from altitude-induced particle population changes; this is attributed at least partially to measurement differences in pitch angle range.

1) Introduction

Energetic particle precipitation (EPP) is known to have a profound impact on nitrogen oxide (NO) [*Rusch et al.*, 1981] and hydroxyl (OH) [*Solomon et al.*, 1981; 1983] production in the stratosphere, mesosphere, and thermosphere. The altitude of production depends on the type and energy of the precipitating particle; larger particles with higher energies penetrate deeper into the atmosphere [e.g., *Jackman*, 1980; *Roble and Ridley*, 1987; *Fang et al.*, 2008; 2010; *Thorne*, 1980]. The NO_x (NO_x = NO + NO_2 + N) catalytic cycle is the primary loss mechanism for ozone (O_3) in the stratosphere above about 24 km [e.g., *Garcia and Solomon*, 1994], while the HO_x (OH + HO_2 + H) catalytic cycle is prevalent in the mesosphere [*Nicolet,* 1975]. Quantifying natural variations in EPP-produced NO_x (EPP-NO_x) and HO_x (EPP-HO_x) and subsequent O_3 destruction is critical to understanding climate effects in the middle atmosphere. Therefore, it is vital that all sources of EPP be identified.

It has long been theorized that Medium Energy Electron precipitation (MEE; ~20 keV to 1 MeV) and relativistic electron precipitation (REP; >1 MeV) might significantly affect the middle atmosphere [*Baker et al.*, 1987]. *Callis et al.* [1991] showed globally integrated increases of EPP-NO_y from MEE and REP of 35-40% from 1979 to 1985 using atmospheric measurements combined with 2D model calculations. NO_y refers to $NO + NO_2 + NO_3 + N_2O_5 + HNO_3 + HO_2NO_2 + ClONO_2$. *Callis et al.* [1998a, 1998b, 2001] used data from the Polar-orbiting Operational Environmental Satellite (POES) Space Environment Monitor version 1 (SEM-1) Medium Energy Proton and Electron Detector (MEPED) and from atmospheric sounders to quantify possible impacts from MEE and REP. Large (>20%) increases that were attributed to EPP-NO_x were observed in stratospheric NO_y near 25 km [*Callis et al.*, 1998a]. Calculations with a 2D transport model using particle input showed an EPP-induced column increase in NO_y from 25-40 km of ~12% [*Callis et al.*, 1998b]. Impacts from MEE and REP are significantly higher in the upper stratosphere above 25 km [*Callis et al.*, 2001]. *Randall et al*. [2001] suggested that EPP-NO_x produced by MEEs led to large stratospheric NO_x enhancements observed at high southern latitudes in September-October 2000, although these enhancements are also consistent with EPP-NO_x production by solar protons [*Jackman et al.*, 2008]. *Randall et al*. [2007] showed that EPP-NO_x comprises up to 10% of stratospheric NO_y globally, and 40% in the polar regions. They further showed that the

EPP Indirect Effect – the production of EPP-NO_x in the mesosphere or lower thermosphere followed by descent to the stratosphere – correlated with both auroral electron and MEE hemispheric power; but they were unable to distinguish between these two sources.

Codrescu et al. [1997] used data from the SEM-1 MEPED instruments to specify MEE-induced ionization in the Thermosphere-Ionosphere-Mesosphere-Electrodynamic General Circulation Model (TIME-GCM). They calculated a 13% increase in HO_x at 78 km near 75°N in January, and an associated 25% decrease in O_3 at the same location. The MEPED data used by *Codrescu et al.* [1997], however, is known to have proton contamination of the electron data channels [*Evans and Greer*, 2000; hereafter referred to as *EG00*]. Beginning with the launch of NOAA-15, a newer version of the MEPED instrument was used as part of the SEM version 2 (SEM-2) and has been launched on seven satellites (NOAA-15, -16, -17, -18, -19, and MetOp-02 (A) and -01 (B)). Details of SEM-2 can be found in *EG00*. The SEM-2 MEPED instrument suffers from the same problems as the SEM-1 MEPED, including cross contamination between electron and proton detectors [*Rodger et al*., 2010a].

There have been several studies that attempted to remove proton contamination from the electron channels in SEM-2 MEPED. One way to remove proton contamination is to produce a differential flux spectrum (e.g., counts sec^{-1} cm^{-2} sr^{-1} keV^{-1}) for protons and then calculate the total contamination that would be observed by the electron channels. *Lam et al*. [2010] assumed a series of exponential functions to fit a proton differential flux spectrum and combined it with the bow-tie method [e.g., *Selesnick and Blake*, 2000] to calculate the total contamination in the electron channels. *Yando et al*. [2011; hereafter referred to as *Y11*] quantified the gathering power for each channel in the SEM-2 MEPED telescopes by simulating the instrument in a field of known particle fluxes and analyzing the response of each channel. *Y11* provided details about the electron detectors' response to protons, allowing a better estimate of proton contamination. The *Y11* gathering powers were experimentally confirmed by *Whittaker et al.* [submitted, 2014], who also showed that the *Lam et al.* [2010] approach for proton contamination correction was effective. However, *Y11* does not provide a proton differential flux spectrum; their results can only be used to calculate contamination if provided with a flux spectrum. *Asikainen and Mursula et al.* [2013] assumed a series of power law spectra to construct a proton differential flux spectrum and applied the response functions from *Y11* to calculate contamination in the electron channels. Neither *Lam et al*. [2010] nor *Asikainen and Mursala* [2013] assessed the error incurred in their calculations by assuming the exponential or power law functional forms, respectively, for the differential flux spectrum; nor did *Codrescu et al*. [1997], who assumed a Maxwellian. In this work we calculate proton and electron differential flux spectra from the SEM-2 MEPED data for each measurement without assuming a single type of spectral function. The resulting spectra have reduced proton contamination, and are accompanied by error bars that account for satellite measurement errors and errors in fitting the spectral distribution. We test the resulting spectra against independent satellite measurements to confirm the validity of our approach. The results of this work provide the necessary data source for accurately modeling the impacts of MEE on the middle atmosphere in future work.

Given the issue of proton contamination noted above, and the fact that the MEPED instruments have sparse coverage in magnetic local time (MLT), there have been several recent attempts to quantify the impacts of MEE indirectly. *Verronen et al*. [2011] and *Andersson et al*. [2012] suggested that mesospheric nighttime OH concentrations could be used as a proxy for MEE precipitation. *Verronen et al*. [2011] based their conclusion on the observation that MEPED 100-300 keV electron count rates and nighttime OH concentrations from 71-78 km and 55°-65° magnetic latitude from the Aura Microwave Limb Sounder (MLS) were highly correlated during March 2005 and April 2006. They found that 56–87% of the OH variation could be explained by EEP. The correlation was weakened by variations in the transport of water vapor, since photolysis of water vapor will perturb the background levels of OH. Similar results were found by *Andersson et al.* [2012], which covered the time period from 2004-2009. Enhanced electron precipitation linked to increased mesospheric OH concentrations has also been correlated with mesospheric ozone depletion [*Andersson et al.*, 2014b]. Another important result was that the MEPED electron channels have high count rates in the South Atlantic Anomaly (SAA) with no correlations to mesospheric OH in the same region [*Andersson et al.*, 2014a], probably due in part to proton contamination. Therefore, although electron precipitation has been observed in the SAA using other methods [e.g., *Pinto and Gonzalez*, 1989], caution is needed when dealing with MEPED data in the SAA.

Another attempt to create a dataset of MEE precipitation and resulting ionization rates that could be used in models is the Atmospheric Ionization Module Osnabruck (AIMOS) model [*Wissing and Kallenrode*, 2009]. AIMOS calculates an electron differential flux spectrum using multiple power law fits to MEPED particle channels. Hemispheric maps of particle flux are produced using statistical correlations between geomagnetic index (Kp) particle fluxes. Unfortunately, the AIMOS model cannot account for errors in the raw MEPED data upon which it is based. In addition, the K_p parameterization introduces errors since MEE will have a time delayed acceleration after a solar storm beyond what is expected by geomagnetic index [*Rodger et al.*, 2010a]. This would only impact fluxes on the short time scales that immediately follow a Solar Proton Event (SPE) and would not have large impacts on longer time scales. Due to the significant direct atmospheric effects caused by MEE [e.g., *Andersson et al.* 2014a; 2014b], and the need to move beyond the current AIMOS treatment of flawed MEPED observations, this paper presents improved data processing which should allow POES SEM-2 MEPED data to be used in chemistry climate models.

In its current form, the POES SEM-2 MEPED MEE data is reported in three integral electron channels, and medium energy protons are reported in five proton broad energy bin channels and one integral proton channel [*Green,* 2013]. This work describes a method that uses the POES SEM-2 MEPED data to define spectral functions for medium energy protons and electrons, remove proton contamination from electron channels, generate a relativistic electron channel, and report an uncertainty value for the fluxes produced.

Section 2 presents the POES SEM-2 MEPED instrument, including issues that currently exist in the data. Section 3 describes the correction method developed to remove proton contamination from the electron channels, and to calculate differential flux spectra for both protons and electrons, along with measurement and correction errors. Section 4 shows results based on the corrected MEPED data along with some comparisons of the corrected data to an independent satellite dataset. Section 5 gives conclusions and outlines topics of future work.

2) POES MEPED Instrument

The POES MEPED instrument used in this work is part of SEM-2, and is described in *EG00* and *Green* [2013]. The MEPED instrument has two proton telescopes and two electron telescopes. One telescope of each particle type is grouped as the 0° detectors and another set is grouped as the 90° detectors. In reality, on POES the 0° detectors are rotated 9° away from zenith (0°) and the 90° detectors are rotated 9° away from the anti-ram direction [*EG00*, figure 2.1.1]. This rotation of the detectors permits a clear field of view for the telescopes. The 0° detectors generally sample a portion of the precipitating energetic particles in the Bounce Loss Cone (BLC) (see Figure A3 of *Rodger et al.* [2010b]). The 90° detectors sample a mix of trapped or precipitating energetic particles depending on their location.

Nominal and effective energy ranges of protons and electrons detected by the MEPED channels are described in *Y11* (their Table 3). The proton telescopes have six energy channels, P1-P6. The electron telescopes have 3 energy channels, E1-E3. Channels P6, E1, E2, and E3 are integral channels; channels P1 through P5 are differential energy channels that measure within a limited energy range. The nominal effective maximum measurement energy for the electron channels is 2.5MeV, while the maximum measurement energy for proton channel P6 is over 200MeV.

The MEPED count rates (counts/sec) used in this study are reported in 16-second intervals, which corresponds to about 100 km along the satellite track, or approximately 1° of geographic latitude at mid-latitudes. The raw data is sampled every other second with a one second integration period [*EG00*] and averaged together to create the 16-second data. A description of the 16-second data can be found in Section 3 of *Codrescu et al.* [1997]. If only one count is identified in an energy channel in a single two-second measurement (one second of measuring by the 90° telescope and one second of measuring by the 0° telescope), this would be reported as one count per second for two seconds. Therefore the minimum non-zero value that can be reported in the 16-second data is two counts per 16 seconds (assuming zero counts are identified in the remaining seven measurements), or 0.125 counts/sec.

There are a number of known issues in the data currently reported by the MEPED instrument. The first issue is the deterioration of the proton telescopes by radiation damage. According to *EG00*, this impact becomes significant after 2-3 years of operation and the effect of this deterioration is to raise the energy thresholds required to register a particle in the telescope. An attempt at fixing this proton channel degradation was shown in *Asikainen et al.* [2012]. In order to assess the proton degradation *Asikainen et al.* [2012] compared measurements when different satellites were in close proximity. This is a reasonable first attempt at assessing potential instrument changes. However, the method is prone to errors because the coincidences are infrequent and only occur at high latitudes where counting statistics are poor. The method also does not account for other circumstances that may affect the measured fluxes such as differences in the pointing direction of the telescopes and the altitude of the satellite. Some studies are underway that statistically compare the satellite measurements over long time periods and give a more reliable estimate of any instrument variation or degradation, but quantitative results are not yet available [*Sandanger et al.*, 2014]. In order to properly validate the impact of the correction applied in this work we do not include a proton degradation correction.

A second known issue with the reported MEPED data is cross-contamination between the proton and electron telescopes. Details on the magnitude of contamination in the nine reported energy channels (P1-P6, and E1-E3) can be found in *Y11*. For the proton detectors, the greatest medium energy electron contamination occurs in channel P1, and decreases at higher energy channels. Channel P5 is the only "pure" channel reported by MEPED, reading only protons and no electrons. Channel P6 has large contamination from relativistic electrons. *Y11* shows that the P6 channel could be used to report quantitative values of relativistic electron precipitation (REP), but this has previously only been used qualitatively [*Miyoshi et al.* 2008; *Evans et al.,* 2008; *Horne et al.* 2009, *Sandanger et al.* 2009; *Millan et al.* 2010; and *Rodger et al.* 2010a]. Protons also contaminate the electron energy channels, E1-E3. Channel E3 is only contaminated by protons with energies exceeding 400keV, while channels E1 and E2 are contaminated by protons with energies exceeding 100keV. Since the contamination of each electron channel varies, the contamination cannot be subtracted out by subtracting one channel from another. The proton contamination in the electron channels E1-E3 is larger than the electron contamination in the proton channels P1-P5. *Y11* (their Appendix B) tabulates the contamination values. The goals of this work are to calculate a correction for proton contamination of the MEPED E1-E3 electron channels, determine relativistic electron count rates to produce a virtual fourth electron channel (E4, 300 keV – 2.5 MeV with a center energy at ~800 keV), use E1-E4 count rates to calculate continuous spectra over the energy range from 25 keV to 10 MeV, and provide realistic error estimates for these spectra.

Note that MEPED also includes Omni-Directional detectors that detect higher energy protons (*EG00*). These detectors were not modeled by *Y11*. Given the different design of the Omni-Directional detectors, it is difficult to quantify the impacts from high energy protons on the MEPED detectors. Any high energy proton contamination that would be detected by the omni-directional detectors is not taken into account in the correction method that follows since this method only uses protons reported by the P1-P6 channels.

3) Proton Contamination Correction

The correction described here is based on the inversion method in *O'Brien and Morley* [2011] and uses weighting functions calculated from geometric factors found in *Y11* (see their Figures 4 and 5). The process of removing proton contamination from the electron channels has three main steps. Step one is to convert data from the proton channels into a proton differential flux spectrum using the inversion method. The second step is to use a forward model to calculate the total proton contamination in the electron channels. In step three the corrected electron channels are put through the inversion method to get the electron differential flux spectrum.

The details and mathematics of the inversion method can be found in Appendix A. The inversion method produces a best fit spectrum, $\vec{f}(E)$, which solves the equation:

$$\vec{y} \approx \vec{\lambda} = \delta t \int_0^\infty \vec{G}(E)\vec{f}(E)dE \tag{1}$$

Here $\vec{y}$ is a vector of measured counts (16-second data in counts per second multiplied by 16 seconds) and $\vec{\lambda}$ is a vector of expected counts from a forward model of the inversion, both with length N_y, the number of channels to be included in the inversion. $\vec{G}$ is a vector of response functions for the instrument channels as a function of energy, *E*, taken here from *Y11* (their Appendix B), and $\vec{f}$ is the differential flux (counts sec^{-1} cm^{-2} sr^{-1} keV^{-1}). δt is the integration time of the instrument data. For this work, the 16 second data was used, and thus δt = 16 seconds. Equation 1 is a simple inversion problem, where $\vec{f}(E)$ is unknown. In discrete form, there are many more unknowns in $\vec{f}(E)$ than equations, where the number of equations is equal to N_y. The forward model in this case is simply calculating $\vec{\lambda}$ by solving Equation 1 using calculated differential flux, $\vec{f}(E)$.

The first step in removing the proton contamination from electrons is to calculate the proton differential flux spectrum. The inversion method described in Appendix A is applied to 5 proton channels, P1-P5, with the assumption of little to no electron contamination. This assumption is not entirely valid in the lower energy proton channels, P1-P4, but the magnitude of the electron contamination compared to proton counts is small compared to the proton contamination of electron channels [*Y11*]. Channel P5 is the only "pure" MEPED channel that has no electron contamination and only detects protons. P6 is left out of the proton inversion since it is highly contaminated by relativistic electrons [*Y11*]. The goal of the inversion method is to minimize the residual of $\vec{y}$ and $\vec{\lambda}$.

The inversion problem described by Equation 1 is unconstrained and needs to be constrained by a possible spectral shape. A spectral shape is calculated by fitting the measurements to a function that combines weighted spectra for energy exponential (EE), power law (PL), single relativistic Maxwellian (RM), and double relativistic Maxwellian (DM) distributions. A graphical example of what these spectra look like alone and when combined can be seen in Figure 1, which shows a representative proton differential flux spectrum for L-Shell 6.15 on 13 May 2003 using data from the NOAA-15 MEPED 0° detector. This particular date and location were chosen arbitrarily simply to demonstrate the inversion method. In Figure 1a, the solid line with 2-sigma error bars (labeled "combined") is the final calculated differential flux spectrum, while the dashed and/or dotted lines are the best fits of the PL, EE, RM, and DM spectra. The error bars include estimates of the contributions from errors in instrument measurement and spectral shape. Figure 1b compares the original proton channel measurements to the results of running a forward model using each spectrum from Figure 1a. Symbols are placed at the estimated measurement center energy for each channel. In this case the proton measurements are fit best with either the combination best fit spectrum or the DM spectrum, not a PL or EE spectrum as is often assumed [e.g. *Asikainen and Mursula et al.*, 2013; *Lam et al.*, 2010].

The combined or DM spectra are generally the best fits among all measurements in 2003 and 2004 (not shown). A forward model is used on the combined best fit spectrum with weighting functions from *Y11* to calculate the proton count contamination in the measured electron counts for each electron channel. The proton contamination is then subtracted from the electron channels, E1-E3, to get uncontaminated electron counts.

A further calculation is also done to create a virtual relativistic electron channel, E4. Since P6 was not included in the calculation of a best proton differential flux spectrum, a forward model can be applied to the proton differential flux to calculate the expected proton counts in the P6 channel. This calculated or "corrected" P6 channel is then subtracted from the original P6 channel. The residual is believed to be the relativistic electron contamination of the P6 channel and is called the E4 channel. The E4 channel acts as an integral channel similar to E3 with a lower energy boundary around 300 keV, but is believed to have a center energy at around 879 keV. As a result the E4 channel is more sensitive to relativistic electrons (> 1 MeV) than the E3 channel. The E4 channel will detect some electrons below 1 MeV and can be compared to gathering power provided by *Y11* for the P6 channel detection of electrons (their Table B2). Therefore, the E4 channel is not a "pure" relativistic electron channel, but does primarily measure > 1 MeV electrons.

Using all the electron channels, E1-E4, an electron differential flux spectrum is calculated a manner similar to that applied to the proton measurements (e.g., by constrained inversion using a best fit spectrum). Figure 2 shows the best electron spectral fits (a) and the same fits run through a forward model along with the original and corrected electron channel outputs (b). This plot is comparable to that seen in Figure 1, except the electron channels in Figure 2b are all integral channels. The error bars in the combined spectrum in Figure 2a include errors in instrument electron measurement and spectral shape; they do not account for errors in the estimate of proton contamination. The best electron differential flux spectrum shown is a combination of all four spectra or the DM. The combined or DM spectra are generally the best fits among all measurements in 2003 and 2004 (not shown). This complete differential flux spectrum can be used by models to provide accurate ionization rates for investigations of the impacts of MEE and REP on the middle atmosphere.

There are some limitations to the correction method described above. This method requires calculated geometric factors, taken here from *Y11*. An assumption that it is safe to interpolate geometric factors linearly in logarithmic energy space is also used. The geometric factors cannot be interpolated to energy ranges above or below those described by *Y11*. This restriction is not a problem at lower energies because the detector design prevents low energy particles (see *Y11* Table 3 for exact values for each detector) from being counted by MEPED [*EG00*]. Contamination of electron channels by protons with energy above 10 MeV cannot be corrected by this method because geometric factors at energies higher than 10 MeV were not calculated in *Y11*. This correction method also provides an estimate of the uncertainties in the generated spectral fluxes that arise from the method itself. The less accurate the assumed spectra used in the method fit to the MEPED channel measurements, the larger the error bars will be on the output spectrum.

The limit at which the error is large enough to remove the data in question is up to the user and depends on the application of the data; however it is not recommended to use data with error bars greater than 200%.

4) Results and Validation

Figure 3 shows the NOAA-17 MEPED 0° detector E3 channel for the original (a) and corrected (b) satellite measurements on the universal time day 29 October 2003 in geographic coordinates. Black measurements are ones where the proton contamination signal was on the same order of magnitude as the original MEE signal (e.g. signal to noise ratio less than or equal to one) and thus no useful electron data could be extracted. During this day a SPE was occurring. Contamination from high energy protons, greater than detected by the P6 channel, shows up as fluxes covering the entire magnetic polar cap (poleward of ~60°N and ~60°S in geographic space). While the correction was able to improve measurements of the radiation belts (areas of maximum electron precipitation), the high energy proton contamination over the magnetic pole could not be removed. This type of contamination only occurs during a large SPE; it is due to very high energy protons that pass through the instrument from all directions and not just the instrument opening. The contamination is extremely difficult to quantify and remove because it would require a complete model of the entire POES/MetOp satellite and its interaction with energetic protons. Such a model is not available; thus, this type of contamination is not accurately removed with the current method. Another region of high energy proton contamination also occurs over the SAA (centered at ~70°W and ~15°S). This region is a zone of weak magnetic field strength where enhanced particle precipitation from the inner radiation belt is believed to occur [*Pinto and Gonzalez*, 1989]. *Andersson et al*. [2014a] has shown that no atmospheric ionization (estimated using mesospheric nighttime OH concentrations) is correlated with enhanced MEPED electron channel count rates in the SAA. Therefore the MEE precipitation shown in the SAA by Figure 3 is likely an artifact of the measurement.

Figures 4 through 6 show the mean daily POES MEPED 0° detector electron channels in L-shell bins with a 0.1 value width for the uncorrected data (Figure 4), corrected data (Figure 5), and ratio of uncorrected to corrected data (Figure 6) for 1 January 2003 through 1 January 2005 in the Southern Hemisphere (SH). Where the ratio in Figure 6 is high, the data correction had the largest impact. These times coincide with SPEs, the most prominent of which in the timeframe shown is the "Halloween Storm" at the end of October 2003. Fluxes over 1000 electrons per second are seen at all L-shells greater than 4 for all electron channels in both the uncorrected (Figure 4) and corrected (Figure 5) data sets. During SPEs, high energy protons above the detection levels of the P6 channel can contaminate electron measurements. These protons are not removed in the current correction method. While some of the high latitude electron flux signal could be real, the more plausible explanation is contamination from high energy protons. These high energy protons can pass through the entire satellite, making their effect on the MEPED telescopes extremely challenging to quantitatively characterize. Thus, their impact is not included in the current correction algorithm.

Enhanced MEE count rates are detected in both the original (Figure 4) and corrected (Figure 5) datasets following solar storms and are not completely removed by the correction method. This is in agreement with other studies [e.g. *Rodger et al.*, 2010a], where radiation belt electrons are accelerated with a time delay from the arrival of a solar storm. The presence of MEE population levels seen in the 0° detector suggests that following a coronal mass ejection (CME) such as that in October 2003, enhanced MEE precipitation can continue to ionize the atmosphere and create NO_x and HO_x in the mesosphere and above. The culmination of this production in the days to weeks following a solar storm could be large, though exactly how large is not known, and is deserving of further study. Approximately 27-day periodic increases in MEE are also apparent in the original (Figure 4) and corrected (Figure 5) datasets. This type of periodic signal was reported by *Blake et al.* [1997] and is likely caused by periodic solar-wind changes related to the Sun's rotation bringing high-speed solar wind streams from coronal holes into an Earth affecting position. This phenomenon was also reported by *Rodger et al.* [2010a].

Next we compare MEPED data to electron spectra from the Detection of Electro-Magnetic Emissions Transmitted from Earthquake Regions (DEMETER) satellite Instrument for Detecting Particles (IDP) [*Sauvaud et al.,* 2006]. DEMETER was launched in June 2004 and flies at an altitude of 670 km in a Sun-synchronous orbit. The IDP is chosen as a comparison measurement due to its higher energy resolution and larger geometrical factor when compared with MEPED. IDP data used here represent the trapped electron population in 128 energy bins spanning 72 keV to 2.3 MeV with bin widths of 17.9 keV. The first and last channels are integral channels measuring all particles less than or more than the specified range, and are thus not used in this work due to difficulties in creating a spectral fit from them [*Whittaker et al.*, 2013]. The IDP is susceptible to contamination by 0.52–2.95 MeV protons [*Sauvaud et al.*, 2013] and therefore the comparisons shown below avoid regions of intense proton fluxes, for example the SAA.

The MEPED comparisons to IDP shown here use the MetOp-02 MEPED data. Only the 90° detectors on MEPED are considered in order to match the IDP viewing direction. Since there are no significant differences between the MEPED 0° and 90° detectors [e.g. EG00; *Y11*], comparison results for the 90° detector pertain to the 0° detector as well. Coincident measurements between MEPED and IDP are defined using the same criteria as *Whittaker et al.* [submitted, 2014]. These criteria are:

- Only measurements above an L-Shell value of 2.5 are considered.
- The absolute difference in time between instrument measurements is less than or equal to 10 minutes.
- The absolute difference in longitude between instrument measurements is less than or equal to 3°.
- The absolute difference in L-Shell values between instrument measurements is less than or equal to 0.5.

In this work, when more than one IDP measurement meets the conditions above with a given MEPED measurement, only the closest coincident IDP measurement in L-Shell value is used. This differs from *Whittaker et al.* [submitted, 2014], which used all coincident measurements. This results in 1862 coincidences between MetOp-02 MEPED and DEMETER IDP during the year 2009.

Figure 7 shows the SH mean coincident electron spectra between L-shell values of 6.0 and 6.25 from IDP (red) and corrected MEPED (black) with dashed red lines and black vertical bars representing one standard mean error in IDP and MEPED respectively. MEPED has the same general shape as the spectrum from IDP, suggesting that the correction method described above is properly modeling the shape of the electron spectrum. MEPED corrected electron differential flux values are on average about twice as large as IDP between 100 keV and 1 MeV. Given a change in magnetic field strength between MetOp-02 (~850 km) and DEMETER (~600 km) altitudes, particle fluxes would be expected to decrease by a factor of ~1.1 using an inverse cubed estimate of magnetic field strength with distance. The approximate factor of two difference between MEPED and IDP is consistent with results from *Whittaker et al.* [submitted, 2014], and is believed to be partially caused by different measured pitch angle ranges.

Figure 8 shows the ratio of differential MEPED flux to coincident differential IDP flux during 2009 at varying L-shells in both hemispheres combined. The year 2009 is used as there were no solar proton events that could corrupt both the MEPED and IDP instruments. Each L-shell bin has a width of 0.25, and measurements with the equivalent of four or fewer detected electron counts by either MEPED or IDP are not included to remove possible noise floor bias. IDP does not report a count rate, so the necessary flux to be above a noise floor of 4 counts is calculated. IDP combines two channels when not in burst mode, thus the noise floor would be four counts in each channel (eight counts total). This occurs over a four second measurement, resulting in a minimum count rate of 2 counts per second. Dividing this count rate by the nominal geometric factor (1.2 cm^2 sr) and energy bin width (17.9 keV) results in the minimum differential flux required to be above the noise floor of four counts (0.0931 counts/sec/cm^2/sr/keV). All L-shells seen in the plot used 15 or more coincident spectra to get average differential flux values. The 1.1 line that marks the expected ratio between MEPED and IDP differential flux based only on changes to magnetic field strength is marked by a black line. At L-shell values above 3.75, MEPED consistently shows greater than expected electron differential flux compared to IDP. Maximum differences occur between 100 keV and 300 keV. Low L-shells (< 3.75) are generally below the expected ratio line (1.1); this is likely caused by lower electron count rates towards the outer edge of the outer belt region. The consistent high bias of MEPED relative to IDP could be due to several factors, including sensitivity of IDP to a broader range of pitch angles than MEPED, a more rapid differential flux decrease with decreasing altitude than predicted by magnetic field strength changes, and/or a spectral shape dependence on L-shell. This latter hypothesis is supported by the variable nature of the comparisons in Figure 8 for different L shells. The observed bias might also be due to residual proton contamination in the MEPED data, but this is unlikely since the comparisons were conducted for a time period of relatively quiet geomagnetic activity.

Figure 9 shows a scatter plot of coincident measurements during 2009 between IDP and corrected MEPED. Points represent integrated electron differential flux (counts cm^{-2} s^{-1}

sr^{-1}) between 100 keV and 300 keV. This energy bin is used since both IDP and MEPED measure it. A black bisector line of slope 1.1 showing the expected increase in flux from IDP to MEPED is drawn for reference. Colors represent the MEPED L-Shell from which the measurement coincidence is taken.

Comparison of corrected MEPED electron fluxes to IDP reveals two distinct populations. One population shows rough agreement between corrected MEPED and IDP, while the second shows significantly reduced electron fluxes in corrected MEPED results at locations of low electron flux identified by both satellites. These measurements occur at low L-Shell values. The population of points near the bisector are in agreement with the results presented by *Whittaker et al.* [submitted, 2014] (their Figure 7).

The reduced MEE population at low L-Shell values in the corrected MEPED data is believed to be an artifact caused by the correction method. When the level of proton contamination is of a similar magnitude to the electron count signal, the correction method will cancel out the electron counts. This will happen when electron counts are very small or proton counts are very high. In the case of a very low electron count (~1 count/sec), noise from the proton channel will be counted as a source of contamination in the electron channel and the correction method will artificially decrease the already small electron count signal. A similar influence from the correction method can be seen at times when proton contamination is much greater than the electron count measurement. For example, electron channel neutralization will occur during a SPE when proton contamination is very large. This is seen by the black colored points in Figure 3. Note that high energy protons, such as those over the polar cap during a SPE, do not get counted as contamination by the correction method and are not removed. Thus any data used during a SPE when proton fluxes are very high, or when the electron signals are very low (e.g. outside the outer Van Allen belt precipitation regions), should be treated with extreme skepticism.

5) Conclusions

In this work a correction method to remove proton contamination from the POES MEPED instrument was applied and compared to coincident measurements from DEMETER IDP. Results from the correction method are:

- Removal of proton contamination from electron channels with the exception of contamination from protons with energies higher than the detection abilities of the P6 channel (> 10 MeV).
- Differential flux from POES MEPED measurements can now be used with error bars for both medium energy protons and electrons (25 keV – 10 MeV).

Analysis of corrected MEPED values reveals:

- Enhanced MEE signals during geomagnetic storms induced by a CME are not caused by proton contamination.
- In some circumstances the correction method can artificially neutralize electron signals when the level of recognized proton contamination is on the same order of magnitude as the original electron signal, such as in the case of very low electron fluxes (e.g., low latitudes) or during very high proton fluxes (e.g., the SAA or during a SPE).

- Electron differential flux reported by MEPED is slightly greater than expected compared to IDP in 2009. The most likely explanations for this are different pitch angle ranges viewed by MEPED and IDP or that differential flux changes with altitude more than is expected by magnetic field strength changes alone.

Future work that could improve this method are as follows:

- Inclusion of a proton channel degradation correction prior to processing by the correction method described in this work.
- Removal of measurements where noise is of the same magnitude as signal in the electron and proton channels.
- More understanding of possible particle differential flux changes with altitude aside from those induced by magnetic field strength differences.

Acknowledgments

We thank P. O'Brien for making his spectral retrieval methods available to the public via SourceForge. Thank you to CNES/CESR Centre de Donnees pour la Physique des Plasmas (CDPP) for providing the DEMETER IDP data. Thank you to the National Oceanic and Atmospheric Administration (NOAA) National Centers for Environmental Information (NCEI, formerly the National Geophysical Data Center (NGDC)) for providing the MEPED data used in this work. Corrected MEPED output and DEMETER IDP data used in this study can be obtained on request from Ethan D. Peck (ethan.peck@lasp.colorado.edu). Original MEPED observations can be obtained from NOAA NCEI at http://ngdc.noaa.gov/stp/satellite/poes/dataaccess.html. Funding for this research came from NSF AGS 1135432 and NASA NNX10AQ54G, NNX14AH54G, and NNX09AI04G.

References

Andersson, M. E., P. T. Verronen, S. Wang, C. J. Rodger, M. A. Clilverd, and B. R. Carson (2012), Precipitating radiation belt electrons and enhancements of mesospheric hydroxyl during 2004–2009, *J. Geophys. Res. Atm.*, *117*(D9), doi:10.1029/2011JD017246

Andersson, M. E., P. T. Verronen, C. J. Rodger, M. A. Clilverd, and S. Wang (2014a), Longitudinal hotspots in the mesospheric OH variations due to energetic electron precipitation, *Atm. Chem. Phys.*, *14*, 1095-1105.

Andersson, M. E., P. T. Verronen, C. J. Rodger, M. A. Clilverd, and A. Seppälä (2014b), Missing driver in the Sun-Earth connection from energetic electron precipitation impacts mesospheric ozone, *Nature Communications*, doi:10.1038/ncomms6197.

Asikainen, T., K. Mursula, and V. Maliniemi (2012), Correction of detector noise and recalibration of NOAA/MEPED energetic proton fluxes, *J. Geophys. Res.*, *117*, A09204, doi:10.1029/2012JA01593.

Asikainen, T., and K. Mursula (2013), Correcting the NOAA/MEPED energetic electron fluxes for detector efficiency and proton contamination, *J. Geophys. Res. Space Physics*, *118*, 6500–6510, doi:10.1002/jgra.50584.

Baker, D. N., J. B. Blake, D. J. Gorney, P. R. Higbie, R. W. Klebesadel, and J. H. King (1987), Highly relativistic magnetospheric electrons: A role in coupling to the middle atmosphere, *Geophys. Res. Lett.*, *14*, 1027.

Barth, C. A., D. N. Baker, K. D. Mankoff, and S. M. Bailey (2001), The northern auroral region as observed in nitric oxide, *Geophys. Res. Lett.*, *28*(8), 1463-1466.

Barth, C. A., K. D. Mankoff, S. M. Bailey, and S. C. Solomon (2003), Global observations of nitric oxide in the thermosphere, *J. Geophys. Res.*, *108*(A1), 1027, doi:10.1029/2002JA009458.

Blake, J. B., D. N. Baker, N. Turner, K. W. Ogilvie, and R. P. Lepping (1997), Correlation of changes in the outer-zone relativistic-electron population with upstream solar wind and magnetic field measurements, *Geophys. Res. Lett.*, *24*(8), 927-929.

Brasseur, G. P., and S. Solomon (2005), Aeronomy of the Middle Atmosphere: Chemistry and Physics of the Stratosphere and Mesosphere, 3rd ed., Springer, Dordrecht, Netherlands.

Callis, L. B., D. N. Baker, J. B. Blake, J. D. Lambeth, R. E. Boughner, M. Natarajan, R. W. Klebesadel, and D. J. Gorney (1991), Precipitating relativistic electrons: Their long-term effect on stratospheric odd nitrogen levels, *J. Geophys. Res.*, *96*(D2), 2939-2976.

Callis, L., M. Natarajan, D. Evans, and J. Lambeth, (1998a), Solar atmospheric coupling by electrons (SOLACE) 1. Effects of the May 12, 1997 solar event on the middle atmosphere, *J. Geophys. Res. Atm.*, *103*(D21),, 28405-28419, doi:10.1029/98JD02408.

Callis, L., M. Natarajan, J. Lambeth, and D. Baker (1998b), Solar atmospheric coupling by electrons (SOLACE) 2. Calculated stratospheric effects of precipitating electrons, 1979-1988, *J. Geophys. Res. Atm.*, *103*(D21),, 28421-28438, doi:10.1029/98JD02407

Callis, L., M. Natarajan, and J. Lambeth (2001), Solar-atmospheric coupling by electrons

(SOLACE) 3. Comparisons of simulations and observations, 1979-1997, issues and implications, *J. Geophys. Res. Atm.*, 106(D7), 7523-7539, doi:10.1029/2000JD900615

Codrescu, M., T. Fuller-Rowell, R. Roble, and D. Evans (1997), Medium energy particle precipitation influences on the mesosphere and lower thermosphere, *J. Geophys. Res. Sp. Phys., 102*(A9), 19977-19987.

Crutzen, P. J. (1970), The influence of nitrogen oxides on the atmospheric ozone content, *Quart. J. Roy. Meteorol. Soc.*, *96*, 320-325.

Evans, D. S, and M. S. Greer (2000), Polar Orbiting Environmental Satellite Space Environmental Monitor-2: Instrument descriptions and archive data documentation, *Tech. Mem.*, Natl. Atmos. And Oceanic Admin., Space Environ. Cent., Boulder, CO.

Evans, D., H. Garrett, I. Jun, R. Evans, and J. Chow (2008), Long-term observations of the trapped high-energy proton population (L < 4) by the NOAA Polar Orbiting Environmental Satellites (POES), *Adv. Space Res.*, *41*(8), 1261–1268, doi:10.1016/j.asr.2007.11.028.

Fang, X., C. E. Randall, D. Lummerzheim, S. C. Solomon, M. J. Mills, D. R. Marsh, C. H. Jackman, W. Wang, and G. Lu (2008), Electron impact ionization: A new parameterization for 100 eV to 1 MeV electrons, *J. Geophys. Res.*, *113*, A09311, doi:10.1029/2008JA013384.

Fang, X., C. E. Randall, D. Lummerzheim, W. Wang, G. Lu, S. C. Solomon, and R. A. Frahm (2010), Parameterization of monoenergetic electron impact ionization, *Geophys. Res. Lett.*, *37*, L22106, doi:10.1029/2010GL045406.

Garcia, R.R., and S. Solomon (1994), A new numerical model of the middle atmosphere 2, Ozone and related species, J. Geophys. Res., 99, 12,937-12,951.

Green J.C. (2013), MEPED Telescope Data Processing Algorithm Theoretical Basis Document, NOAA NGDC.

Gu, X., Z. Zhao, B. Ni, Y. Shprits, and C. Zhou (2011), Statistical analysis of pitch angle distribution of radiation belt energetic electrons near the geostationary orbit: CRRES observations, *J. Geophys. Res.*, *116*, A01208, doi:10.1029/2010JA016052.

Horne, R. B., M. M. Lam, and J. C. Green (2009), Energetic electron precipitation from the outer radiation belt during geomagnetic storms, *Geophys. Res. Lett.*, *36*, L19104, doi:10.1029/2009GL040236.

Jackman, C., J. Frederick, and R. Stolarski (1980), Production of odd nitrogen in the stratosphere and mesosphere: An intercomparison of source strengths, *J. Geophys. Res.*, *85*, 7495–7505.

Jackman, C. H., et al. (2008), Short- and medium-term atmospheric constituent effects of very large solar proton events, Atmos. Chem. Phys. 8, 765-785.

Lam, M. M., R. B. Horne, N. P. Meredith, S. A. Glauert, T. Moffat-Griffin, and J. C. Green (2010), Origin of energetic electron precipitation >30 keV into the atmosphere, *J. Geophys. Res.*, *115*, A00F08, doi:10.1029/2009JA014619.

Millan, R. M., K. B. Yando, J. C. Green, and A. Y. Ukhorskiy (2010), Spatial distribution of relativistic electron precipitation during a radiation belt depletion event, *Geophys. Res. Lett.*, *37*, L20103, doi:10.1029/2010GL044919.

Miyoshi, Y., K. Sakaguchi, K. Shiokawa, D. Evans, J. Albert, M. Connors, and V.

Jordanova (2008), Precipitation of radiation belt electrons by EMIC waves, observed from ground and space, *Geophys. Res. Lett.*, *35*, L23101, doi:10.1029/2008GL035727.

Nicolet, M. (1975), Stratospheric ozone: An Introduction to its study, *Reviews of Geophysics and Space Physics*, *13*(5), 593-636.

O'Brien, T. P., and S. K. Morley (2011), Documentation of C Inversion Library, from the *IRBEM* library, <irbem.sourceforge.net>.

Pinto, O., Jr., and W. D. Gonzalez, Energetic electron precipitation at the South Atlantic Magnetic Anomaly: a review (1989), J. Atmos. Terr. Phys., 51, 351-365.

Randall, C. E., D. E. Siskind, and R. M. Bevilacqua (2001), Stratospheric NO_x enhancements in the southern hemisphere vortex in winter/spring of 2000, Geophys. Res. Lett. 28 (12), 2385-2388.

Randall, C. E., V. L. Harvey, C. S. Singleton, P. F. Bernath, C. D. Boone, and J. U. Kozyra (2006), Enhanced NO_x in 2006 linked to strong upper stratospheric Arctic vortex, *Geophys. Res. Lett.*, 33, L18811, doi:10.1029/2006GL027160.

Randall, C. E., V. L. Harvey, C. S. Singleton, S. M. Bailey, P. F. Bernath, M. Codrescu, H. Nakajima, and J. M. Russell III (2007), Energetic particle precipitation effects on the Southern Hemisphere stratosphere in 1992–2005, *J. Geophys. Res.*, 112, D08308, doi:10.1029/2006JD007696.

Randall, C. E., V. L. Harvey, D. E. Siskind, J. France, P. F. Bernath, C. D. Boone, and K. A. Walker (2009), NOx descent in the Arctic middle atmosphere in early 2009, Geophysical Research Letters, 36 (18), L18811, doi:10.1029/2009GL039706.

Roble, R. G., and E. C. Ridley (1987), An auroral model for the NCAR thermospheric general circulation model (TGCM), Ann. Geophys., 5A, 369.

Rodger, C. J., M. A. Clilverd, J. C. Green, and M. M. Lam (2010a), Use of POES SEM-2 observations to examine radiation belt dynamics and energetic electron precipitation into the atmosphere, *J. Geophys. Res.*, *115*, A04202, doi:10.1029/2008JA014023.

Rodger, C. J., B. R. Carson, S. A. Cummer, R. J. Gamble, M. A. Clilverd, J.-A. Sauvaud, M. Parrot, J. C. Green, and J.-J. Berthelier (2010b), Contrasting the efficiency of radiation belt losses caused by ducted and non-ducted whistler mode waves from ground-based transmitters, *J. Geophys. Res.*, *115*, A12208, doi:10.1029/2010JA015880.

Rusch, D., J. Gerard, S. Solomon, P. Crutzen, and G. Reid (1981), The effect of particle precipitation events on the neutral and ion chemistry of the middle atmosphere -I. Odd nitrogen, *Planet. Space Sci., 29*(7), 767-774 , doi:10.1016/0032-0633(81)90048-9.

Sandanger, M., F. Søraas, M. Sørbø, K. Aarsnes, K. Oksavik, and D. Evans (2009), Relativistic electron losses related to EMIC waves during CIR and CME storms, *J. Atmos. Sol. Terr. Phys.*, *71*, 1126–1144, doi:10.1016/j.jastp.2008.07.006.

Sandanger, M., L.-K. G. Ødegaard, H. N. Tyssøy, J. Stadsnes, F. Søraas, and K. Oksavik (2014), A new method of recalibrating NOAA MEPED proton measurements, *EGU General Assembly*, Vienna, Austria, April.

Sauvaud, J.-A., T. Moreau, R. Maggiolo, J. Treilhou, C. Jacquey, A. Cros, J. Coutelier, J. Rouzard, E. Penou, and M. Gangloff (2006), High-energy electron detection onboard DEMETER: The IDP spectrometer, description and first results on the inner belt., *PSS*, *54*(5), doi:10.1016/j.pss.2005.10.019.

Sauvaud, J.-A., M. Walt, D. Delcourt, C. Benoist, E. Penou, Y. Chen, and C. T. Russell (2013), Inner radiation belt particle acceleration and energy structuring by drift resonance with ULF waves during geomagnetic storms, J. Geophys. Res. Space Physics, 118, 1723–1736, doi:10.1002/jgra.50125.

Selesnick, R. S., and J. B. Blake (2000), On the source location of radiation belt relativistic electrons, *J. Geophys. Res.*, *105*(A2), 2,607-2,624.

Solomon, S., D.W. Rusch, J.-C. Gérard, G.C. Reid, and P.J. Crutzen (1981), The effect of particle precipitation events on the neutral and ion chemistry of the middle atmosphere: II. Odd Hydrogen, *Planet. Space Sci*., 29, 8, 885-592.

Solomon, S., P. J. Crutzen, and R. G. Roble (1982), Photochemical coupling between the thermosphere and the lower atmosphere 1. Odd nitrogen from 50 to 120 km, *Journal of Geophysical Research*, *87*(C9), 7206-7220.

Solomon, S., G. C. Reid, D. W. Rusch, and R. J. Thomas (1983), Mesospheric ozone depletions during the solar proton event of July 13, 1982, II, Comparison between theory and measurements, *Geophys. Res. Lett.*, *10*, 257-260.

Thorne, R. M. (1980), The importance of energetic particle precipitation on the chemical composition of the middle atmosphere, *Pure Appl. Geophys., 118*, 129-151.

Vampola, A. L. (1998), Outer zone energetic electron environment update, in Conference on the High Energy Radiation Background in Space, 128–136, IEEE Press, Piscataway, N. J.

Verronen, P. T., C. J. Rodger, M. A. Clilverd, and S. Wang (2011), First evidence of mesospheric hydroxyl response to electron precipitation from the radiation belts, *J. Geophys. Res. Atm.*, *116*, D07307, doi:10.1029/2010JD014965

Whittaker, I. C., R. J. Gamble, C. J. Rodger, M. A. Clilverd, and J.-A. Sauvaud (2013), Determining the spectra of radiation belt electron losses: Fitting DEMETER IDP observations for typical and storm-times, *J. Geophys. Res.*, doi:10.1002/2013JA019228

Wissing, J. M., and M.-B. Kallenrode (2009), Atmospheric Ionization Module Osnabruck (AIMOS): A 3-D model to determine atmospheric ionization by energetic charged particles from different populations, *J. Geophys. Res.*, *114*, A06104, doi:10.1029/2008JA013884.

Yando, K., R. M. Millan, J. C. Green, and D. S. Evans (2011), A Monte Carlo simulation of the NOAA POES Medium Energy Proton and Electron Detector instrument, *J. Geophys. Res.*, *116*, A10231, doi:10.1029/2011JA016671.

Figure Captions

Figure 1: (a) Differential flux of medium energy protons (black solid line), along with the best fit spectra for PL, EE, RM, and DM in counts/sec/cm^2/sr/keV. Two sigma standard error of the combined flux spectrum is denoted by vertical bars. (b) Original and calculated channel count rates (counts/sec) using spectra from (a). Channels are marked at their estimated measurement center energies as opposed to nominal energies. Data is taken at an L-Shell value of 6.15 from NOAA-15 0° detector on 13 May 2003.

Figure 2: (a) Differential flux of medium energy electrons (black solid line), along with the best fit spectra for PL, EE, RM, and DM in counts/sec/cm^2/sr/keV. Two sigma standard error of the combined flux spectrum is denoted by vertical bars. (b) Original, corrected, and calculated integral channel count rates (counts/sec) using spectra from (a). Channels are marked at their estimated measurement center energies as opposed to nominal energies. Data is taken at an L-Shell value of 6.15 from NOAA-15 0° detector on 13 May 2003.

Figure 3: NOAA-17 MEPED 0° detector E3 channel (>300 keV) during a SPE on 29 October 2003 with original values (a) and corrected values (b). Black measurements denote measurements with too much contamination to extract a corrected signal. Points in the SAA are likely also invalid due to high energy proton contamination that is not accounted for in the correction method.

Figure 4: Daily average SH original MEPED 0° detector integrated flux channels E1, E2, E3, and P6 in L-shell and time for 1 January 2003 through 1 January 2005 measured in counts/second.

Figure 5: Same as Figure 4 but for corrected MEPED 0° detector integrated flux channels E1, E2, E3, and E4.

Figure 6: Ratio of Figure 5 to Figure 6, original E1, E2, E3, and P6 divided by corrected E1, E2, E3, and E4.

Figure 7: Average of SH coincidence measurement spectra from DEMETER IDP (red) and MetOp-02 MEPED (black) in 2009 at L-shell values between 6.0 and 6.25. Dashed red lines and black vertical bars represent one mean standard error for IDP and MEPED respectively.

Figure 8: Ratio of average electron differential flux between MetOp-02 MEPED and DEMETER IDP coincidences during 2009 for L-shell bins with width 0.25. Coincident spectra are taken from both the NH and SH and a minimum of 15 spectra were required for each L-shell bin. All measurements were required to have more than four electron counts as would be detected by the instrument before conversion to differential flux. A black line representing the expected ratio of MEPED to IDP based on changes to magnetic field strength using an inverse cubed relation has been placed at a value of 1.1.

Each colored line represents an L-shell bin with the lower edge of the bin marked in the color bar.

Figure 9: Scatter plot of integrated electron differential flux from 100-300 keV for all coincident measurements between DEMETER IDP and MetOp-02 in the year 2009. Comparisons are shown between IDP and corrected MEPED measurements. Points are colored by associated L-Shell value. Black line is a slope of 1.1for reference.

Appendix A

What follows here is the mathematical inversion method developed by *O'Brien and Morley* [2011] and adapted for use with the POES MEPED data. The goal of the method is to solve Equation 1:

$$\vec{y} \approx \vec{\lambda} = \delta t \int_0^{\infty} \vec{G}(E)\vec{f}(E)dE \tag{1}$$

Equation 1 can be discretized towards a numerical solution using the following equations:

$$\vec{y} \approx \vec{\lambda} = \underline{\underline{H}}\,\vec{f} \tag{A1}$$

$$H_{ij} \approx \delta t G_i(E_j)\Delta E_j \tag{A2}$$

$$f_j = f(E_j), \tag{A3}$$

where $\vec{y}$ and $\vec{\lambda}$ are the observed and expected MEPED channel counts, $\underline{\underline{H}}$ is the inversion weighting function derived from the modeling results of *Yando et al.* [2011] with dimensions $N_y \times N_E$ and units of cm^2 sr sec keV, N_Y is the number of MEPED channels (indexed with i), N_E is the number of output energy bins (indexed with j), and f_j is the discretized form of $f(E)$ from Equation 1 with units of counts/cm^2/sr/sec/keV. Equation A1 is a classic underdetermined, unconstrained, inversion equation. There are N_E unknown variables in $\vec{f}$ and N_y equations, where N_y is less than N_E. The inversion technique that follows adds constraints to Equation A3 by taking a weighted average of possible spectral distributions to minimize the difference between $\vec{y}$ and $\vec{\lambda}$ in Equation A1. The energy bins used in this inversion method are logarithmically separated in energy. The calculation of ΔE_j in Equation A2 comes from calculating the difference of energies at bin edges.

A "penalty" function is defined to measure the likelihood of seeing the observed counts,

$\vec{y}$, given the calculated expected counts, $\vec{\lambda}$. In other words, the penalty function is a calculation of how far apart $\vec{y}$ and $\vec{\lambda}$ are from each other including possible measurement errors. Observations and expected counts can differ due to various possible measurement error processes. We use Poisson and calibration errors as the only two possible measurement error processes in this correction method. The probability distribution for Poisson errors and calibration errors (given by a Gaussian distribution), are defined as:

$$p^{(P)}(y|\lambda) = \frac{\lambda^y e^{-\lambda}}{y!} \tag{A4}$$

$$p^{(C)}(y|\lambda) = \frac{\exp\left[-((\ln y - \ln\lambda)/\delta y)^2/2\right]}{\sqrt{2\pi}\, y\delta y}, \tag{A5}$$

where $p^{(P)}$ is the Poisson probability distribution of y given λ and $p^{(C)}$ is the Calibration probability distribution of y given λ.

The penalty function is defined as the negative natural log of the probability distribution. Terms that are not dependent on λ are grouped together as a general constant. The penalty functions for Equations A4 and A5 are defined as:

$$\ell^{(P)}(\lambda) = -\ln p^{(P)} = \lambda - y ln(\lambda) + \text{constants} \tag{A6}$$

$$\ell^{(C)}(\lambda) = -\ln p^{(C)} = ((\ln y - \ln\lambda)/\delta y)^2/2 \; + \text{constants}, \tag{A7}$$

where $\ell^{(P)}$ is the Poisson probability distribution penalty function, $\ell^{(C)}$ is the calibration probability distribution penalty function, and δy is the Gaussian relative error, calculated to be 0.4 [*Green*, 2013] from bowtie analysis [*Selesnick and Blake*, 2000] for POES MEPED.

The derivatives and second derivatives of equations A6 and A7 with respect to λ will be needed later and are as follows:

$$\frac{d\ell^{(P)}}{d\lambda} = 1 - y/\lambda \tag{A8}$$

$$\frac{d^2\ell^{(P)}}{d\lambda^2} = y/\lambda^2 \tag{A9}$$

$$\frac{d\ell^{(C)}}{d\lambda} = (\ln\lambda - \ln y)/(\delta y)^2/\lambda \tag{A10}$$

$$\frac{d^2\ell^{(C)}}{d\lambda^2} = (1 + \ln y - \ln\lambda)/(\lambda\delta y)^2 \tag{A11}$$

Only one penalty function is used in this work for a given value of y. Therefore we select the larger source of error from either the Poisson counting error, $1/\sqrt{y}$, or the calibration Gaussian relative error, δy:

$$\ell_i = \begin{cases} \ell^{(P)} & y < (\delta y)^{-2} \\ \ell^{(C)} & \text{otherwise} \end{cases} \tag{A12}$$

The summation of the selected penalty function from Equation A12 is a measure of how likely a spectral distribution, $\vec{f}$, appropriately describes the original channel measurements, $\vec{y}$. Therefore, the goal of this inversion method is to minimize the following equation:

$$\ell(\vec{\lambda}) = \sum_i \ell_i(\lambda_i) \tag{A13}$$

Converting the MEPED measurements into differential flux is inherently an unconstrained problem. To constrain the solution, this inversion method assumes a set of possible spectra and then weights each spectrum based on its ability to minimize Equation A13. Each spectral distribution is defined by a vector of free parameters, q, and the total number of free parameters in each distribution is defined as N_q, where N_q is less than N_E. This effectively reduces the number of unknowns in the inversion of Equation A1. We use four spectral distributions to constrain our solution: power law (PL), energy exponential (EE), single relativistic Maxwellian (RM), and double relativistic Maxwellian (DM).

The PL spectrum, $f^{(\mathrm{PL})}$, requires two free parameters to fit (e.g. $N_q = 2$). We will need each spectral distribution along with its derivatives and second derivatives with respect to each free parameter. These equations are described as follows:

$$f^{(\mathrm{PL})}(E) = \exp(q_1 - q_2 \ln E) \tag{A14}$$

$$\frac{\partial f^{(\mathrm{PL})}}{\partial q_1} = f^{(\mathrm{PL})} \tag{A15}$$

$$\frac{\partial f^{(\mathrm{PL})}}{\partial q_2} = -\ln(E) f^{(\mathrm{PL})}(E) \tag{A16}$$

$$\frac{\partial^2 f^{(\mathrm{PL})}}{\partial q_1^2} = f^{(\mathrm{PL})} \tag{A17}$$

$$\frac{\partial^2 f^{(\mathrm{PL})}}{\partial q_1 q_2} = -\ln E\, f^{(\mathrm{PL})} = \frac{\partial^2 f^{(\mathrm{PL})}}{\partial q_2 q_1} \tag{A18}$$

$$\frac{\partial^2 f^{(\mathrm{PL})}}{\partial q_2^2} = (\ln E)^2\, f^{(\mathrm{PL})}, \tag{A19}$$

The EE spectrum is described by the following equations with two free parameters:

$$f^{(\mathrm{EE})}(E) = \exp(q_1 + q_2 E) \tag{A20}$$

$$\frac{\partial f^{(\mathrm{EE})}}{\partial q_1} = f^{(\mathrm{EE})} \tag{A21}$$

$$\frac{\partial f^{(\mathrm{EE})}}{\partial q_2} = E f^{(\mathrm{EE})} \tag{A22}$$

$$\frac{\partial^2 f^{(\mathrm{EE})}}{\partial q_1^2} = f^{(\mathrm{EE})} \tag{A23}$$

$$\frac{\partial^2 f^{(\mathrm{EE})}}{\partial q_1 q_2} = E f^{(\mathrm{EE})} = \frac{\partial^2 f^{(\mathrm{EE})}}{\partial q_2 q_1} \tag{A24}$$

$$\frac{\partial^2 f^{(\mathrm{EE})}}{\partial q_1^2} = E^2 f^{(\mathrm{EE})} \tag{A25}$$

The RM spectrum has two free parameters and is described by the following equation, while it has derivatives as described by equations A21-A25 if $f^{(\mathrm{EE})}$ is replaced by $f^{(\mathrm{RM})}$:

$$f^{(\mathrm{RM})}(E) = E(1 + E/E_0/2)\exp(q_1 + q_2 E) \tag{A26}$$

The DM spectrum has four free parameters as described below and has the same derivatives as the RM spectrum with similar derivatives for the two additional free parameters:

$$f^{(\mathrm{DM})}(E) = E(1 + E/E_0/2)[\exp(q_1 + q_2 E) + \exp(q_3 + q_4 E)] \tag{A27}$$

The final step is to calculate the fit errors and combine the individual spectra to create a best multiple spectral fit. For a given spectrum, $f^{(k)}(E)$, the best fit is the minimization of $\ell^{(k)}(\vec{\lambda})$ with respect to $\vec{q}^{(k)}$, yielding best fit free parameters, $\hat{q}^{(k)}$. For this case, k can be PL, EE, RM, or DM. The minimization routines require derivatives of $\ell^{(k)}$ with respect to $\vec{q}^{(k)}$, given by:

$$\frac{\partial \ell}{\partial q_m} = \sum_i \frac{\partial \ell_i}{\partial \lambda_i} \sum_j \frac{\partial \lambda_i}{\partial f_j} \frac{\partial f_j}{\partial q_m} = \sum_i \frac{\partial \ell_i}{\partial \lambda_i} \sum_j H_{ij} \frac{\partial f_j}{\partial q_m} \tag{A28}$$

To compute the error bars for a given spectral fit, the second derivative of the penalty function with respect to each free parameter is necessary. This can be represented by a Hessian using each combination of free parameters in the following form:

$$\frac{\partial^2 \ell}{\partial q_m \partial q_{m'}} = \sum_i \frac{\partial^2 \ell_i}{\partial \lambda_i^2} \sum_j H_{ij} \frac{\partial f_j}{\partial q_m} \sum_{j'} H_{ij'} \frac{\partial f_{j'}}{\partial q_{m'}} + \sum_i \frac{\partial \ell_i}{\partial \lambda_i} \sum_j H_{ij} \frac{\partial^2 f_j}{\partial q_m q_{m'}} \qquad \text{(A29)}$$

We assume that the error of the retrieved flux is distributed log-normally with a standard deviation given by the following expression:

$$\begin{aligned} \sigma_{\ln f^{(k)}(E)} &= \sqrt{\sum_m \sum_{m'} \frac{\partial \ln f^{(k)}}{\partial q_m^{(k)}} \operatorname{cov}(q_m^{(k)}, q_{m'}^{(k)}) \frac{\partial \ln f^{(k)}}{\partial q_{m'}^{(k)}}} \\ &= \sqrt{\sum_m \sum_{m'} \frac{1}{f^{(k)}} \frac{\partial f^{(k)}}{\partial q_m^{(k)}} \operatorname{cov}(q_m^{(k)}, q_{m'}^{(k)}) \frac{1}{f^{(k)}} \frac{\partial f^{(k)}}{\partial q_{m'}^{(k)}}} \end{aligned} \qquad \text{(A30)}$$

$$\operatorname{cov}\left(q_m^{(k)}, q_{m'}^{(k)}\right) = \begin{pmatrix} & \vdots & \\ \cdots & \dfrac{\partial^2 \ell^{(k)}}{\partial q_m \partial q_{m'}} & \cdots \\ & \vdots & \end{pmatrix}^{-1} \qquad \text{(A31)}$$

To combine the multiple spectra into a single best fit spectrum we calculate a weighting, *w*, for each spectrum based on the penalty function, $\ell^{(k)}$, and number of free parameters, N_q:

$$w_k = \frac{\exp(-\ell^{(k)} - N_q^{(k)})}{\sum_k \exp(-\ell^{(k)} - N_q^{(k)})} \qquad \text{(A32)}$$

Finally, the weighted spectra are summed together to yield the following best-fit combined spectrum, $\hat{f}(E)$, with normalized error, $\delta \ln \hat{f}(E)$:

$$\ln \hat{f}(E) = \langle \ln f^{(\text{combined})}(E) \rangle = \sum_k w_k \ln f^{(k)}(E) \qquad \text{(A33)}$$

$$\delta \ln \hat{f}(E) = \sqrt{\operatorname{var} \ln f^{(\text{combined})}(E)}$$

$$= \sqrt{\sum_k w_k \left(\sigma^2_{\ln f^{(k)}(E)} + \ln^2 f^{(k)}(E)\right) - \langle \ln f^{(\text{combined})}(E)\rangle^2} \tag{A34}$$

To convert this into differential particle flux and the standard error on that flux the following equations are applied:

$$\hat{f}(E) = \exp\left(\ln \hat{f}\,(E)\right) \tag{A35}$$

$$\hat{\sigma}(E) = \hat{f}(E) \cdot \delta \ln \hat{f}(E) \tag{A36}$$

Appendix B: Table of Variables

Variable	Units	Description
$\vec{y}$	Counts (#)	Vector of measured counts from POES MEPED with length N_y.
N_y	Channels	Number of energy channels from POES MEPED used in inversion.
$\vec{\lambda}$	Counts (#)	Vector of expected counts calculated by inversion method.
E	keV	Energy
$\vec{G}(E)$	cm^2 sr	Vector of response functions for POES MEPED energy channels at particle energy, *E*, from *Y11* appendix B.
$f(E)$	#/cm^2/sr/sec/keV	Differential particle flux at energy, *E*.
δt	sec	Integration time of instrument data in use. 16 seconds for this work.

$\underline{\underline{H}}$	cm^2 sr sec keV	Weighting function of inversion with dimensions $N_y \times N_E$
N_E	Bins	Number of energy bins used in discretization.
f_j	#/cm^2/sr/sec/keV	Discretized form of *f*(*E*) from equation 1.
$p^{(P)}$	Unitless	Poisson probability distribution of y given λ.
$\ell^{(P)}$	Unitless	Poisson probability distribution penalty function.
$p^{(C)}$	Unitless	Calibration probability distribution of y given λ.
$\ell^{(C)}$	Unitless	Calibration probability distribution penalty function.
δy	Unitless	Gaussian relative error
$\vec{q}$	Unitless	Vector of free parameters for each spectrum of length N_q.
N_q	parameters	Number of free parameters for a given spectrum. This

		equals 2 for PL, EE, and RM or 4 for DM.
E_0	keV	Particle rest energy: 511 for electrons and 9.38×10^5 for protons.
$\sigma_{\ln f^{(k)}(E)}$	$\ln(\#/cm^2/s/sr/keV)$	Standard error on flux of log-normal distribution spectrum.
w_k	Unitless	Weighting on a given spectrum contribution towards the total combined spectrum.
$\hat{f}(E)$	$\#/cm^2/s/sr/keV$	Combined differential particle flux.
$\hat{\sigma}(E)$	$\#/cm^2/s/sr/keV$	Standard error on combined differential particle flux.
$E_D(\alpha)$	$\#/cm^2/s/sr/keV$	Differential Particle Flux per pitch angle.
E_F	$\#/cm^2/s/keV$	Differential Particle Flux over entire BLC.
L	Unitless	L-Shell value
Λ	degrees	Magnetic Latitude

911

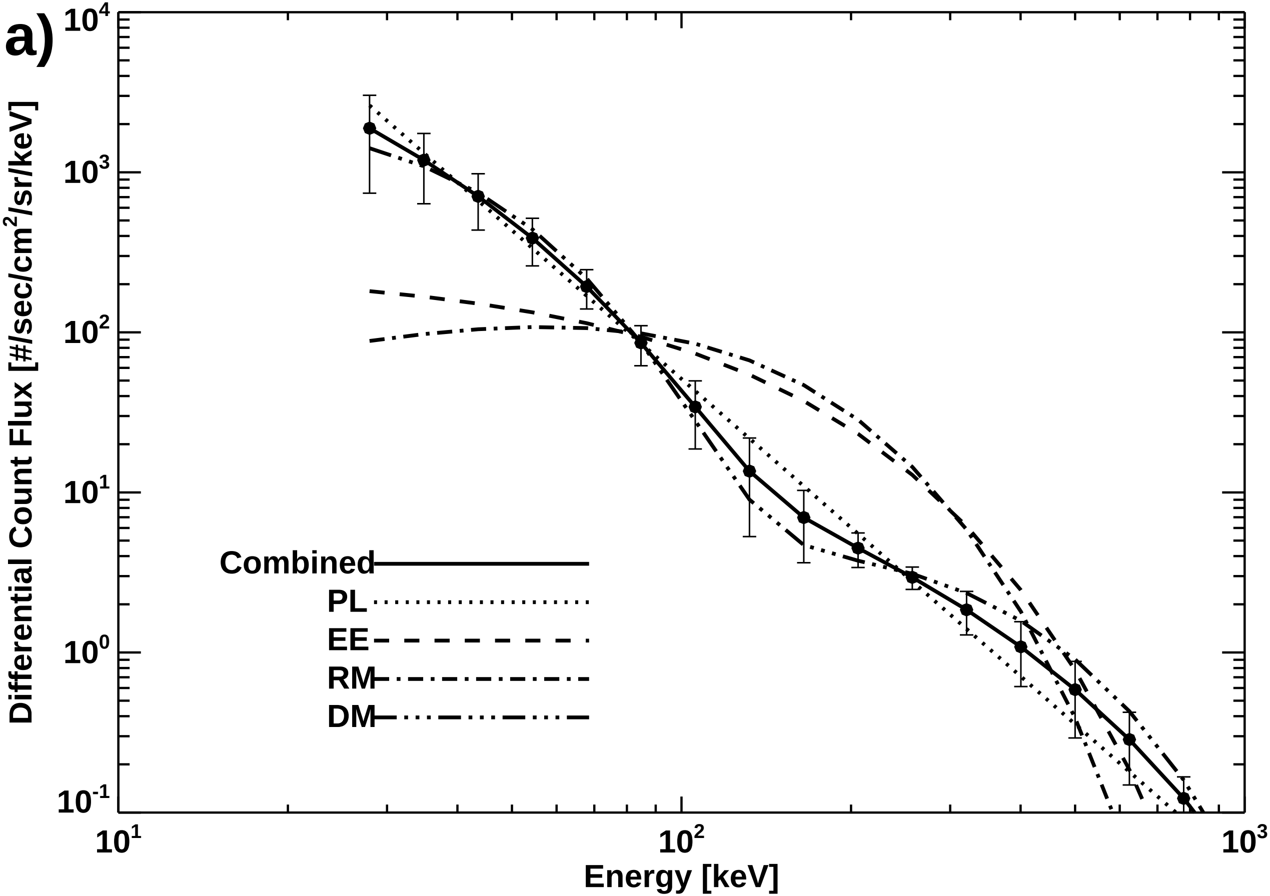

a)
Differential Count Flux [#/sec/cm^2/sr/keV]
10^4
10^3
10^2
10^1
10^0
10^{-1}
10^1
10^2
10^3
Energy [keV]
Combined
PL
EE
RM
DM

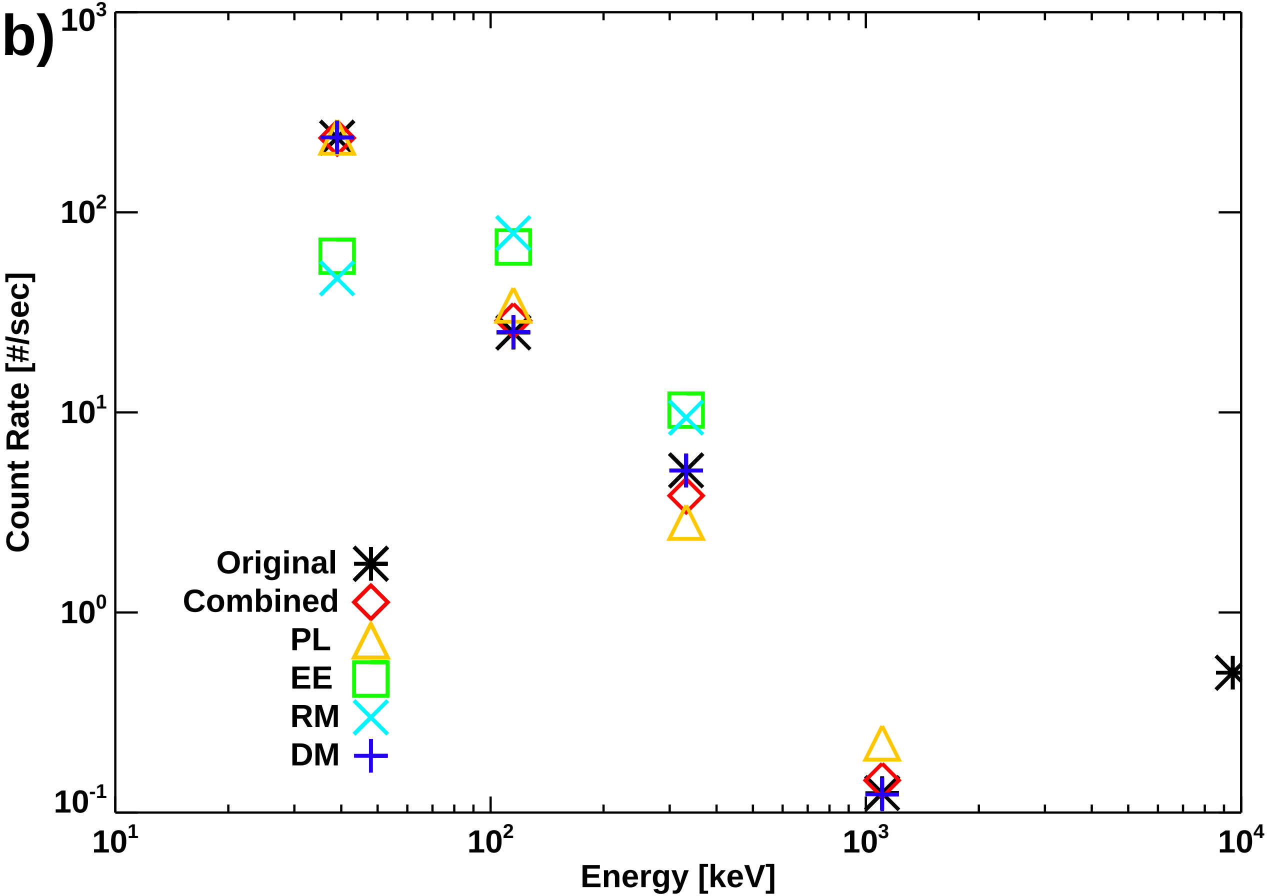
b)
Count Rate [#/sec]
10^{3}
10^{2}
10^{1}
10^{0}
10^{-1}
10^{1}
10^{2}
10^{3}
10^{4}
Energy [keV]
Original
Combined
PL
EE
RM
DM

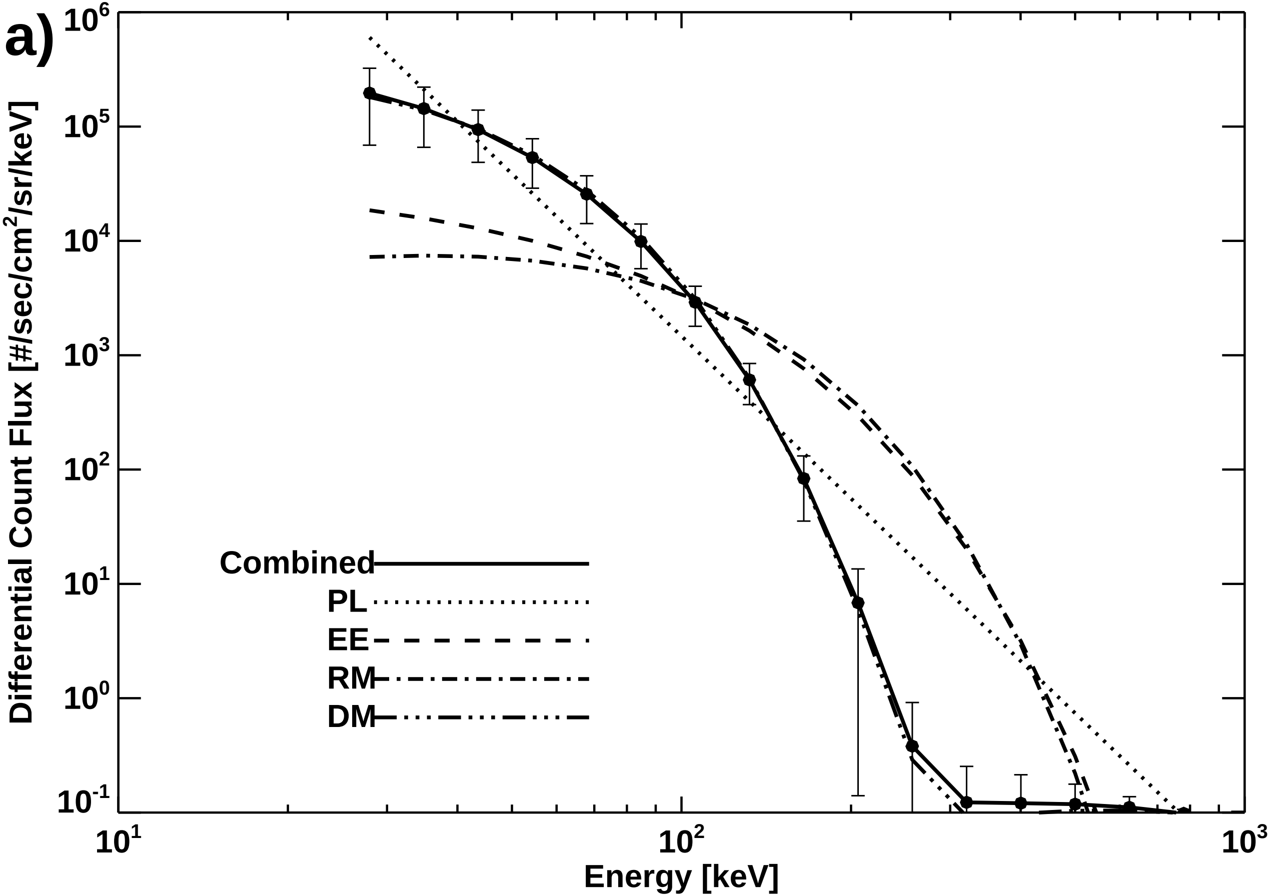
a)
Differential Count Flux [#/sec/cm^2/sr/keV]
10^6
10^5
10^4
10^3
10^2
10^1
10^0
10^{-1}
10^1
10^2
10^3
Energy [keV]
Combined
PL
EE
RM
DM

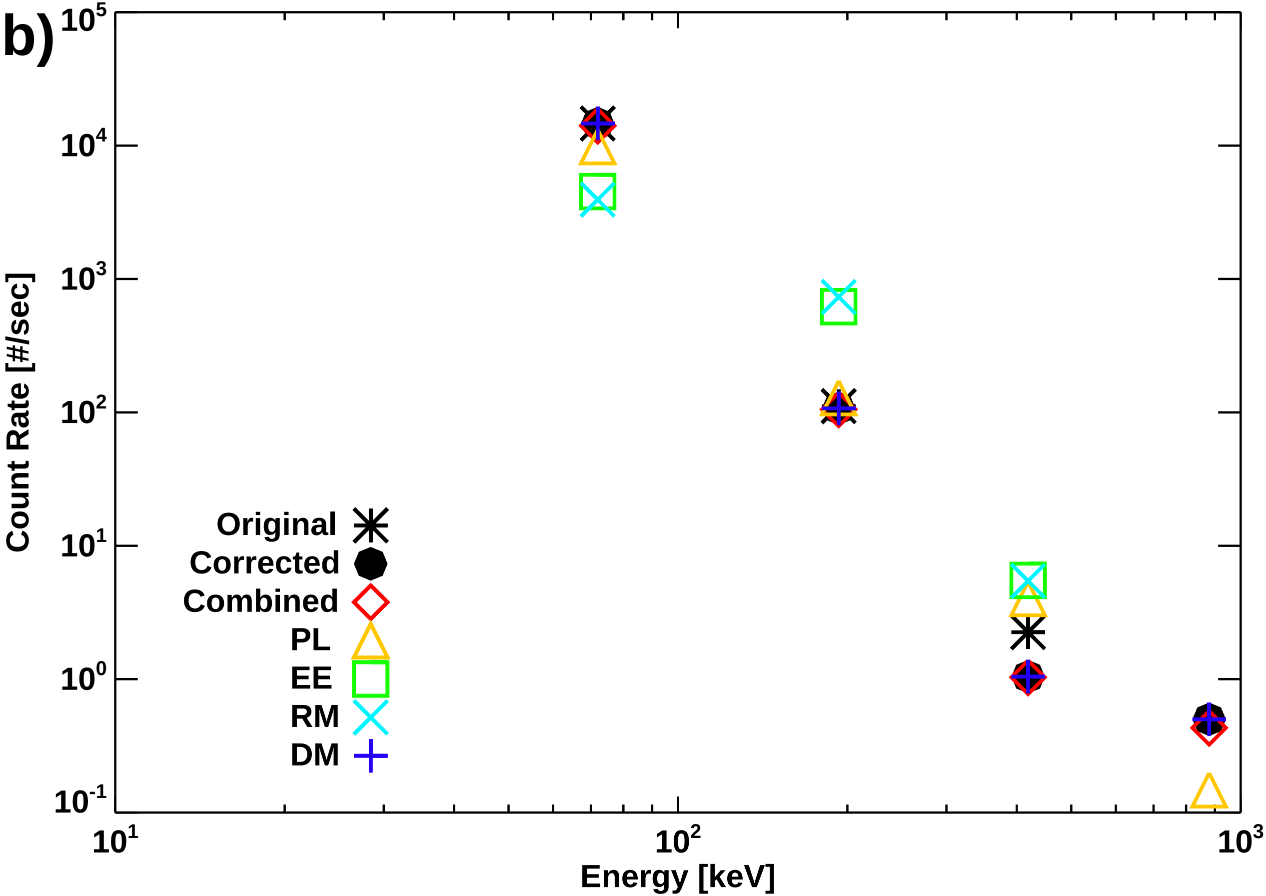

b)
10^5
10^4
10^3
10^2
10^1
10^0
10^{-1}
Count Rate [#/sec]
10^1
10^2
10^3
Energy [keV]
Original
Corrected
Combined
PL
EE
RM
DM

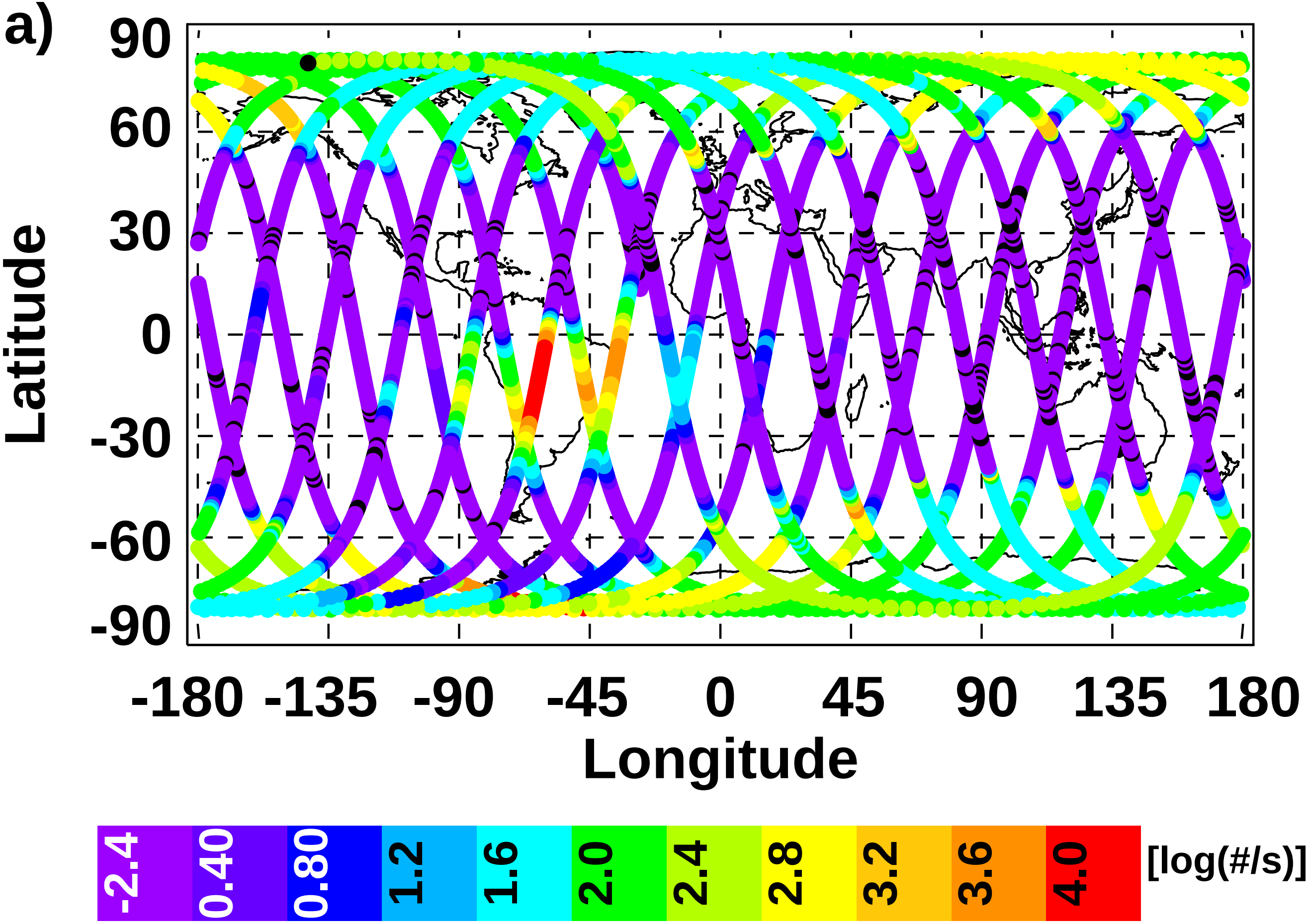

a)
Latitude
90
60
30
0
-30
-60
-90
-180
-135
-90
-45
0
45
90
135
180
Longitude
-2.4
0.40
0.80
1.2
1.6
2.0
2.4
2.8
3.2
3.6
4.0
[log(#/s)]

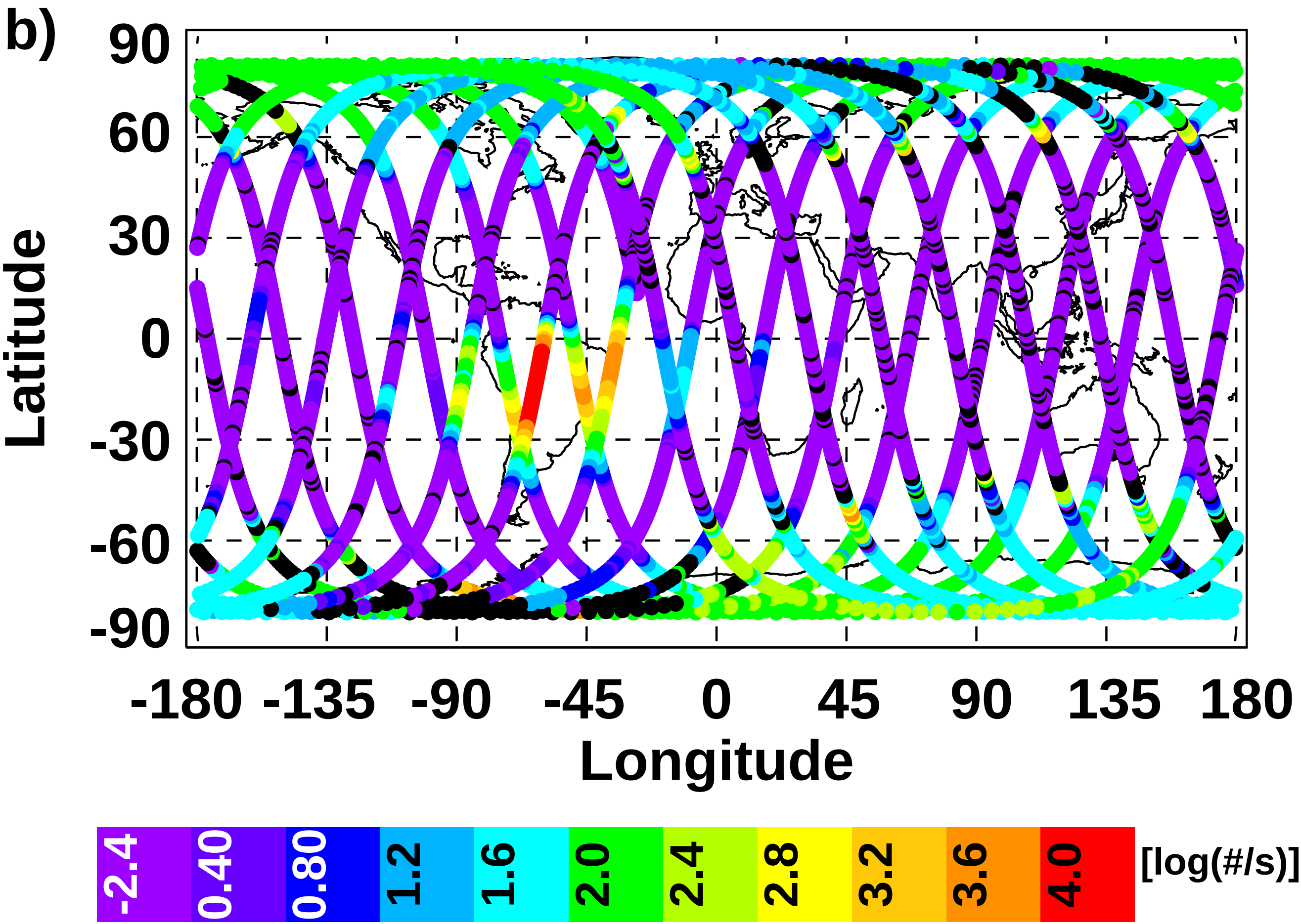
b)
90
60
30
0
-30
-60
-90
Latitude
-180
-135
-90
-45
0
45
90
135
180
Longitude
-2.4
0.40
0.80
1.2
1.6
2.0
2.4
2.8
3.2
3.6
4.0
[log(#/s)]

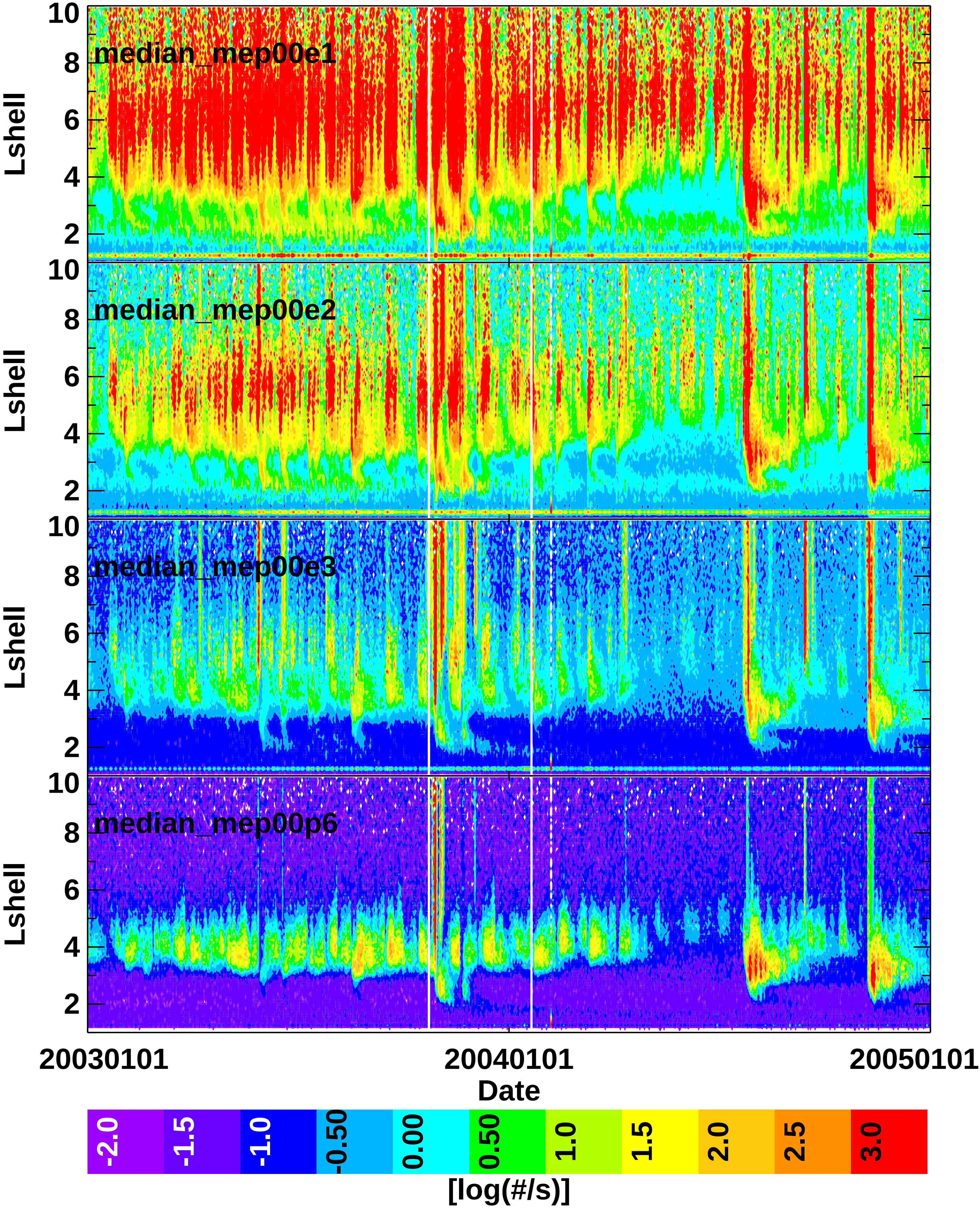
median_mep00e1
median_mep00e2
median_mep00e3
median_mep00p6
Lshell
10
8
6
4
2
20030101
20040101
20050101
Date
-2.0
-1.5
-1.0
-0.50
0.00
0.50
1.0
1.5
2.0
2.5
3.0
[log(#/s)]

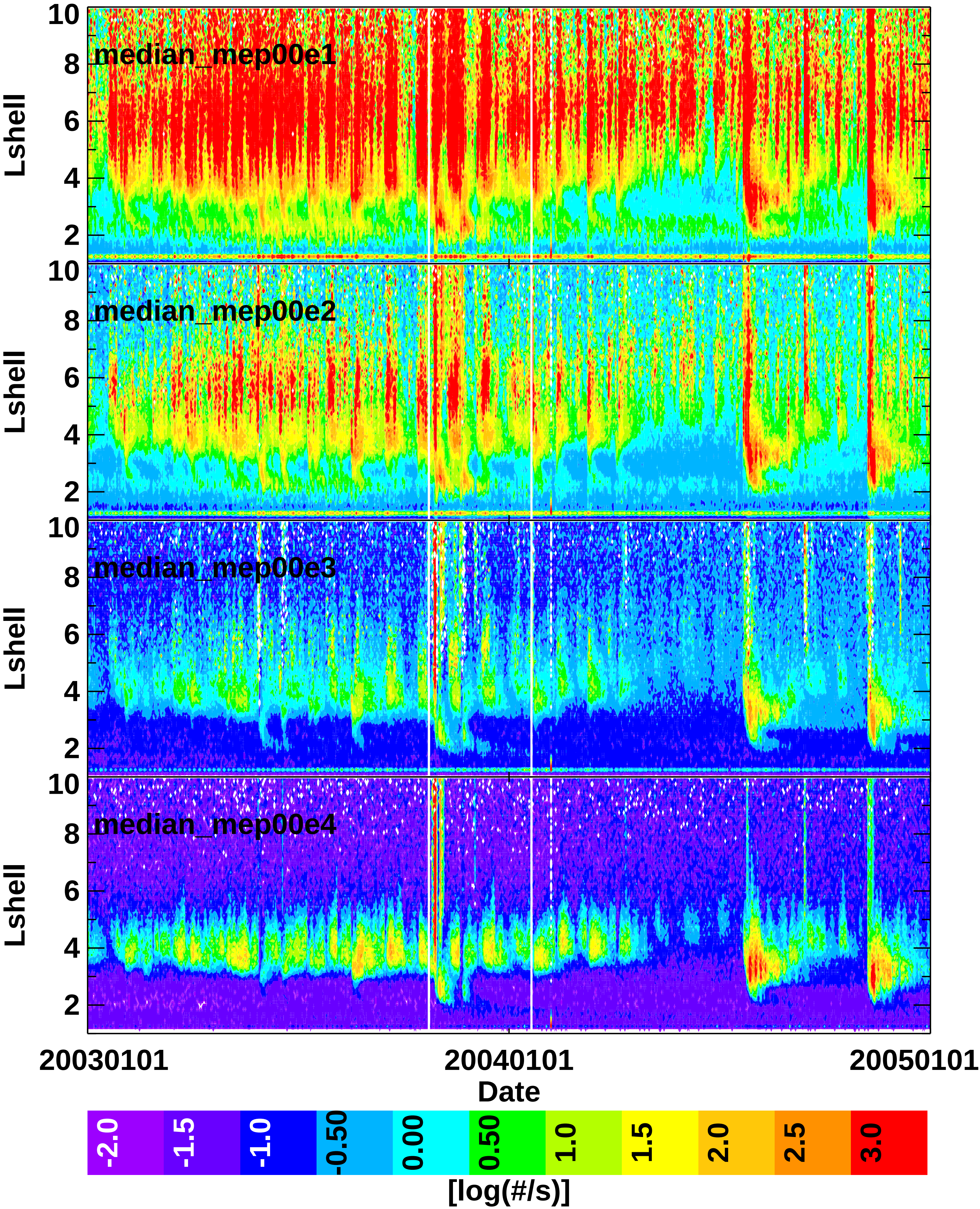

median_mep00e1
median_mep00e2
median_mep00e3
median_mep00e4
Lshell
10
8
6
4
2
20030101
20040101
20050101
Date
-2.0
-1.5
-1.0
-0.50
0.00
0.50
1.0
1.5
2.0
2.5
3.0
[log(#/s)]

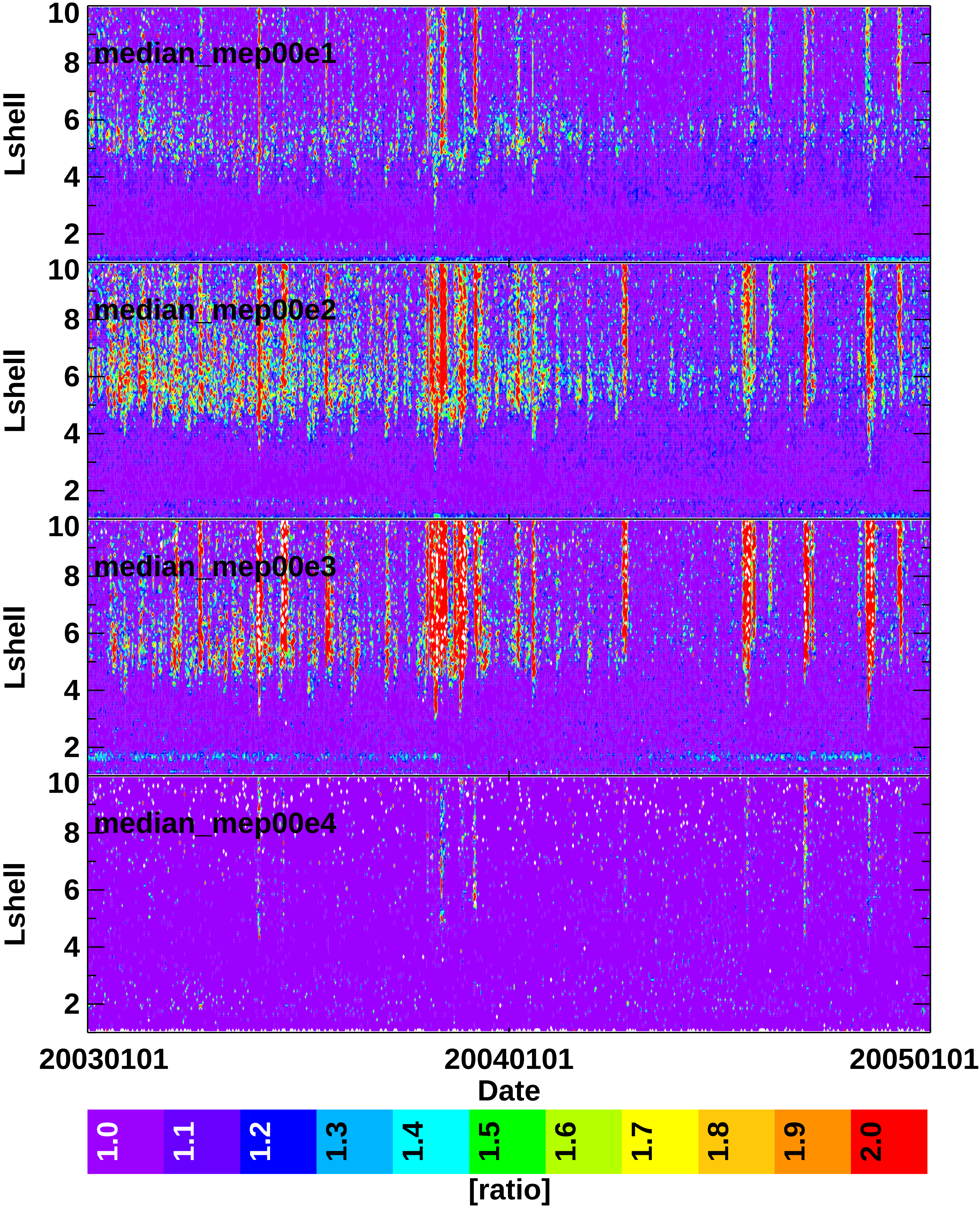
median_mep00e1
median_mep00e2
median_mep00e3
median_mep00e4
Lshell
10
8
6
4
2
20030101
20040101
20050101
Date
1.0
1.1
1.2
1.3
1.4
1.5
1.6
1.7
1.8
1.9
2.0
[ratio]

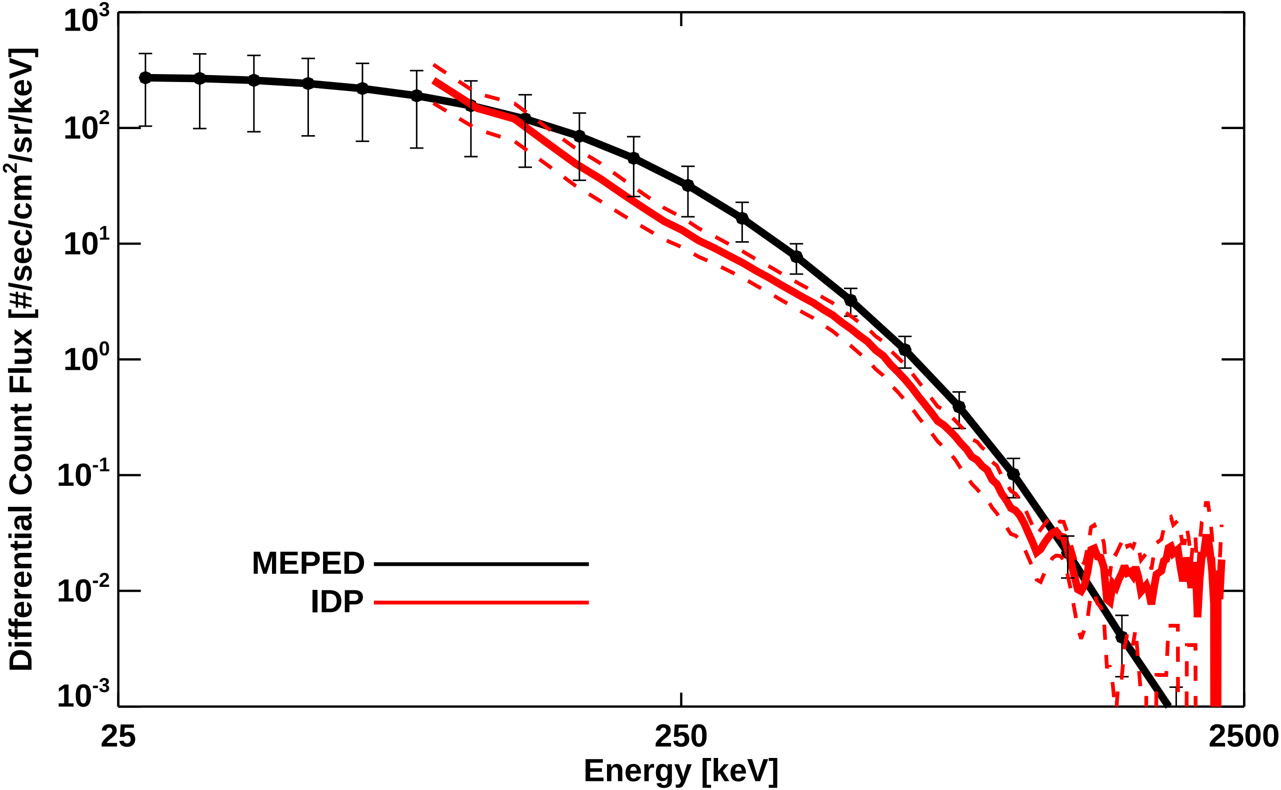

Differential Count Flux [#/sec/cm^2/sr/keV]
10^3
10^2
10^1
10^0
10^{-1}
10^{-2}
10^{-3}
MEPED
IDP
25
250
2500
Energy [keV]

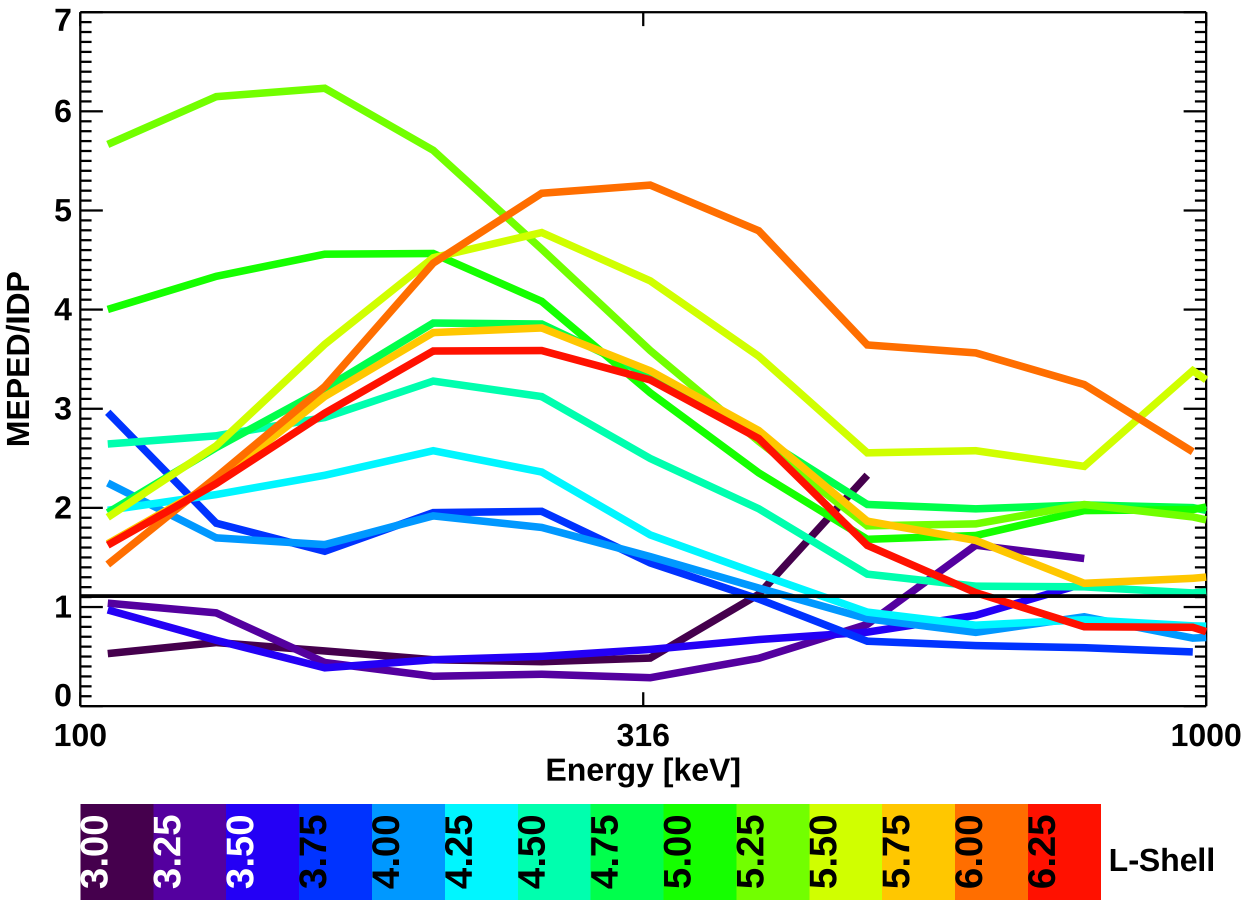

MEPED/IDP
7
6
5
4
3
2
1
0
100
316
1000
Energy [keV]
3.00
3.25
3.50
3.75
4.00
4.25
4.50
4.75
5.00
5.25
5.50
5.75
6.00
6.25
L-Shell

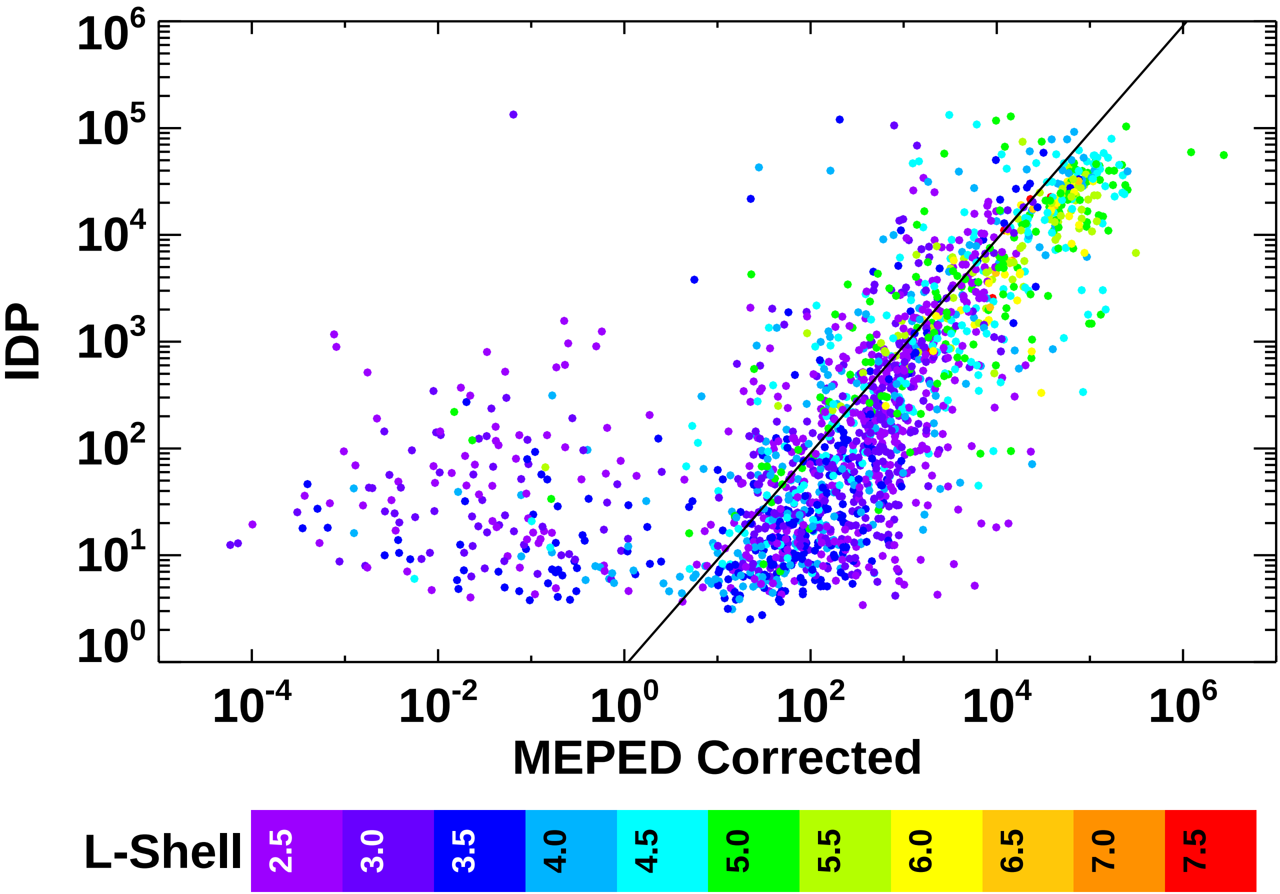

IDP
MEPED Corrected
10^{0} 10^{1} 10^{2} 10^{3} 10^{4} 10^{5} 10^{6}
10^{-4} 10^{-2} 10^{0} 10^{2} 10^{4} 10^{6}
L-Shell
2.5 3.0 3.5 4.0 4.5 5.0 5.5 6.0 6.5 7.0 7.5